

Testing Gravity with MeerKAT and the SKA



**UNIVERSITY *of the*
WESTERN CAPE**

Author: Mponeng Kopana

Supervisor: Prof. Roy Maartens

Co-Supervisor: Dr. Sheean Jolicoeur

Department of Physics and Astronomy
University of the Western Cape

Year: 2020

Declaration of Authorship

- I, Mponeng Kopana (3983539), hereby declare that I know what plagiarism entails, namely to use anothers work and to present it as my own without attributing the sources in the correct way.
- I know that plagiarism is a punishable offence because it constitutes theft.
- I understand the plagiarism policy of the Faculty of Natural Science of the University of the Western Cape.
- I know what the consequences will be if I plagiarise in any of the assignments for my course.
- I declare therefore that all work presented by me for every aspect of my course, will be my own, and where I have made use of anothers work, I will attribute the source in the correct way.

UNIVERSITY OF THE WESTERN CAPE

Abstract

Faculty of Science
Department of Physics and Astronomy

The new 64-dish radio telescope array MeerKAT will be absorbed into the international Square Kilometre Array (SKA) in late 2020s. These two telescope arrays will produce three-dimensional maps of the integrated intensity of the 21cm emission from neutral hydrogen in galaxies, out to redshifts of 1.5 and 3 respectively. These maps contain a signature of the growth of large-scale structure in the Universe. This signature can be uncovered via redshift space distortions of the two-point correlation function, or power spectrum, of the 21cm brightness temperature fluctuations. The growth rate governs the amplitude of the anisotropic signal from redshift-space distortions. It is a powerful probe of gravity and its measurement has the potential to test whether general relativity holds. We use models of the 21cm intensity and its power spectrum, starting from a simple linear model of redshift-space distortions and then extending to nonlinear models. With these models, we make Fisher forecast predictions of the precision with which MeerKAT and the SKA can measure the growth rate.

Acknowledgements

I sincerely thank both my supervisors; Prof. Roy Maartens and Dr. Sheean Jolicoeur for their patience, tolerance, availability, understanding, guidance and honesty. Roy Maartens thanks agian to be like a father guider by pushing me but in a polite way to become committed to my work also helping with calculations and giving a picture of what are we measuring in the project. Sheean was like a brother to me, sharing idea s on how to work hard and being energized on work and guiding me on technical computational issues, such as applying PYTHON script with CLASS.

I'm very grateful for the opportunity to attend SARAO Bursary Conference in December 2019, There I benefited from interaction a Masters student Warren Naidoo from UKZN, who adviced me on learning basics of cosmological concepts and with Dr. Jacinta Delhaize, who shared her thoughts on skills for scientist. Last but not least, Dr. Moumita Aich from UKZN during my poster session gave me useful comments.

During my emotional times I thank Piet Mahlatse Magwele from Mankweng Youth Development (MYD) from Limpopo Province for his ideas on how to work on my errors and building my confidence on my own. How could I forget Reikantseone Diretse a Masters student from UCT being my inspiration for publishing a paper during his first year Masters, rectifying my grammar, pronunciation, I mean my English teacher as a whole, he was always being there for me.

List of Figures

1.1	The comoving, luminosity and angular diameter distances as functions of redshift for the standard cosmological model, using the best-fit parameters of Planck 2018 [7]	5
1.2	Evolution of the energy densities: radiation, matter and dark energy (Λ) against scale factor a (from [8]).	8
1.3	Evolution of dimensionless densities Ω_i in Λ CDM with Planck 2018 best-fit parameters. Critical redshift of z_{eq} (matter–radiation equality) is also shown in dashed dotted vertical line.	11
2.1	Growth suppression factor for Λ CDM and EdS.	22
2.2	Evolution of LCDM growth rate.	24
2.3	The matter transfer function at redshift $z = 0.1$ computed using CLASS [9]. The black dashed line represents k at equality.	28
2.4	The matter power spectrum P_m computed using CLASS. The solid lines are the linear power spectrum while the dashed lines that are shown on small scales (large k) are the non-linear power implemented by the HALOFIT option in CLASS. The dash dotted vertical line k_{H_0} (red) and dashed line k_{eq} (black) are also shown.	29
2.5	Linear (solid) and non-linear (dotted line) model of the dimensionless matter power spectrum at $z = 0$	30
2.6	The average brightness temperature against z	33
2.7	The HI intensity bias against z	34
3.1	The diagram above is the relation between real and redshift space on linear to non linear scales [20].	36
3.2	The HI damping parameter against z	40
3.3	Multipoles of the observed linear galaxy power spectrum at $z = 0.0, 0.5, 1.0, 1.5$, left to right, top to bottom. Blue, red and black lines represent the monopole, quadrupole and hexadecapole respectively. Dash-dotted black line is the equality scale.	42

3.4	Impact of RSD on the HI power spectrum at redshifts 0 (top-left), 1 (top-middle), 2 (top-right), 3 (bottom-left), 4 (bottom-middle) and 5 (bottom-right). Simulations are compared to the linear model. The upper part of each panel shows the HI power spectrum (monopole) in real space (red) and redshift space (blue). The bottom part displays the ratio between the monopoles in redshift and real space (solid black) and the prediction of linear theory (dashed black). RSD enhance/ suppress power on large/ small scales. Linear theory can explain the HI clustering in redshift space down to very small scales at high-redshift, while it cannot at low redshift on the scales we probe in the simulations. (From [22].)	43
3.5	Multipoles of the HI power spectrum at $z = 0.1$ with Gaussian FoG damping, using (3.18), which determines k_D (black dash-dot line).	45
3.6	Colour map of linear HI power spectrum in real space (<i>left</i>) and redshift space (<i>right</i>) at $z = 0.1$. Black lines are iso-power contours.	46
3.7	Colour map of HI power spectrum with a Gaussian (<i>left</i>) and Lorentzian (<i>right</i>) damping factor, at $z = 0.1$	47
4.1	Power spectrum multipoles of HI intensity mapping using SKA Band 1 at redshift $z = 0.5$. The multipoles without the beam and foreground cut effect, represented in dashed lines and multipoles with both effects (beam and foreground cut) represented in solid lines.	51
4.2	The fundamental mode function (<i>left</i>) and volume function (<i>right</i>) against bin redshift.	53
4.3	The noise power spectra for MeerKAT in L-Band and UHF-Band (<i>left</i>) and SKA in Bands 1 and 2 (<i>right</i>).	54
4.4	System temperature for MeerKAT.	57
4.5	The SNR of the HI intensity power spectrum for the MeerKAT surveys in L Band (top panels) and UHF Band (bottom panels). The left panels show SNR per redshift bin; the right panels show the cumulative SNR at each redshift bin. Blue lines include only the FoG effects, without beam or foreground effects. With beam effects included, we have the red lines and with foreground effects added to beam effects, we get the black lines.	58
4.6	System temperature for SKA in Bands 1 and 2.	60
4.7	The SNR of the HI intensity power spectrum for the SKA surveys in Band 1 (top panels) and Band 2 (bottom panels). The left panels show SNR per redshift bin; the right panels show the cumulative SNR at each redshift bin. Blue lines include only the FoG effects, without beam or foreground effects. With beam effects included, we have the red lines and with foreground effects added to beam effects, we get the black lines.	61
4.8	The SNR of HI intensity mapping with MeerKAT and SKA1 survey (left panel) and cumulative SNR (right panel).	61

5.1	For MeerKAT and SKA: the forecast marginalized errors for γ , per redshift bin (<i>left</i>) and cumulative (<i>right</i>).	64
5.2	For MeerKAT and SKA: the forecast marginalized errors for $\sigma_{8,0}$, per redshift bin (<i>left</i>) and cumulative (<i>right</i>).	64
5.3	The dotted lines show the improvement in marginalised errors compared to Figures 5.1 and 5.2 with $N_d = 84$ dishes in MeerKAT.	66
5.4	The percentage difference between MeerKAT of 64 and extend MeerKAT of 84 dishes.	67
5.5	For MeerKAT and SKA: normalized marginal errors on γ and $\sigma_{8,0}$	68

Abbreviations

Acronym	What (it) Stands For
BAO	Baryon Acoustic Oscillations
EFE	Einstein Field Equations
CMB	Cosmic Microwave Background
DES	Dark Energy Survey
EdS	Einstein-de-Sitter
EoS	Equation of State
FLRW	Friedmann-Lemaître-Robertson-Walker
GR	General Relativity
IM	Intensity Mapping
MeerKAT	Karoo Array Telescope
ΛCDM	Lambda Cold Dark Matter
2PCF	2-Point Correlation Function
RSD	Redshift Space Distortions
SKA	Square Kilometre Array
LCDM	Lambda Cold Dark Matter
BBN	Big Bang Nucleosynthesis

Contents

Declaration of Authorship	i
Abstract	ii
Acknowledgements	iii
List of Figures	iv
Abbreviations	vii
1 Introduction	1
1.1 Friedmann-Lemaitre-Robertson-Walker Spacetime	3
1.2 Content of the Universe	6
1.3 Background Dynamics	9
2 Cosmological Perturbations for Large-Scale Structure	13
2.1 Perturbation of Conservation Equations	16
2.2 Perturbation of Einstein Field Equations	19
2.3 Evolution of Perturbations	21
2.4 Power Spectrum	27
2.5 Galaxy and HI Intensity Mapping Surveys	31
3 Redshift Space Distortions of HI Intensity Mapping	35
3.1 Linear Redshift Space Distortions	35
3.2 Nonlinear Redshift Space Distortions	39
3.3 Multipole expansion of power spectrum	41
3.4 HI power spectrum in \mathbf{k} -space	46
4 Measuring the Redshift-space Power Spectrum with MeerKAT and SKA	48
4.1 Modelling the Power Spectrum	49
4.2 Signal to Noise of the Power Spectrum	52
4.3 Signal to Noise for MeerKAT	56
4.4 Signal to Noise for SKA	59

5 Fisher Forecasts for MeerKAT and SKA	62
5.1 Fisher Forecast Formalism	63
5.2 Extended MeerKAT	66
5.3 Normalized Marginal Errors	68
6 Conclusions and Future Work	70
6.1 Summary	70
6.2 Future Work	73
Bibliography	74

Chapter 1

Introduction

Here we give a brief overview of the relevant features of the background model of the Universe. We draw on a range of sources [1–6]

Standard cosmology is based on the Cosmological Principle, that the universe, at each fixed cosmic time, is homogeneous means no preferred direction and isotropic means no preferred position. It is only applicable when averaging over large enough cosmic scales. On these scales, the Universe is effectively smooth. The energy densities of matter and radiation, together with the expansion rate of the Universe, are then purely time-dependent, according to the Cosmological Principle. Furthermore, the curvature of constant-time hypersurfaces is constant. This averaged model is the cosmological background, which is a Friedmann-Lemaitre-Robertson-Walker (FLRW) spacetime.

When we study the background spacetime, there are two things that need to be considered: the energy densities ρ_i of the different components of the Universe and the Hubble rate of expansion,

$$H(t) = \frac{\dot{a}(t)}{a(t)}, \quad (1.1)$$

Here t is the cosmic time – it is the unique proper time variable such that $t = \text{constant}$ hypersurfaces are homogeneous and isotropic. The scale factor a

is dimensionless and it tracks the growth in the physical ('proper') separation of free-falling particles and in the wavelength of propagating photons:

$$\mathbf{r}(t) = a(t) \mathbf{r}_0, \quad \lambda(t) = a(t) \lambda_0. \quad (1.2)$$

We are free to fix the scale factor at one time, and we choose the time today, t_0 . Then we take

$$a_0 \equiv a(t_0) = 1. \quad (1.3)$$

Then in (1.2), \mathbf{r}_0 is the separation today (often called the 'comoving' separation) and λ_0 is the wavelength today – i.e. the wavelength measured by a fundamental observer.

The redshift z of photons is defined by the ratio of the observed wavelength to the emitted wavelength:

$$1 + z = \frac{\lambda_0}{\lambda(t)} = \frac{1}{a(t)}, \quad (1.4)$$

where we used (1.2). This equation allows us to translate between a and z when considering photon emitters from the past ($t_{\text{emit}} = t < t_0$). The Hubble constant is often given in terms of a dimensionless constant h :

$$H_0 = 100h \text{ km s}^{-1} \text{ Mpc}^{-1} = \frac{h}{2998} \text{ Mpc}^{-1} = \frac{h}{9.78} \text{ Gyr}^{-1}, \quad (1.5)$$

where we choose units such that the speed of light is $c = 1$. The current best-fit value of h from Planck 2018 cosmic microwave background (CMB) measurements is [7]

$$h = 0.6766. \quad (1.6)$$

1.1 Friedmann-Lemaître-Robertson-Walker Space-time

The FLRW metric is given by

$$ds^2 = -dt^2 + \frac{a(t)^2}{(1 + K|\mathbf{x}|^2/4)} \delta_{ij} dx^i dx^j, \quad (1.7)$$

where the K is the constant curvature of $t = \text{constant}$ hypersurfaces. From now on we will assume flat spatial sections, i.e., $K = 0$, which is consistent with current cosmological observations [7]. It is useful to define a conformal time η , so that the metric becomes

$$ds^2 = a^2 [-d\eta^2 + \delta_{ij} dx^i dx^j], \quad \eta = \int \frac{dt}{a(t)}. \quad (1.8)$$

Then we can define a conformal Hubble parameter

$$\mathcal{H} = \frac{a'}{a} = aH, \quad (1.9)$$

where a prime denotes $d/d\eta$.

The comoving line-of-sight distance to an emitter at redshift z is

$$\chi(z) = \int_0^z \frac{dz'}{H(z')}. \quad (1.10)$$

The physical distance of the emitter from the observer's world-line at the time of emission is $a(t)\chi$, where $a(t)$ is given by (1.4). The physical distance today is then χ .

The other measures of distance in the expanding universe are based on observations of ‘standard candles’, e.g. supernovae of type Ia, and of ‘standard rulers’, e.g. baryon acoustic oscillation (BAO) features in the distribution of galaxies. The

luminosity distance is given by

$$d_L(z) = (1+z) \int_0^z \frac{dz'}{H(z')} . \quad (1.11)$$

If we know the luminosity of a source, we can measure its luminosity distance and then we have information on the Hubble rate. The angular diameter distance is given by

$$d_A(z) = \frac{1}{(1+z)} \int_0^z \frac{dz'}{H(z')} = \frac{d_L(z)}{(1+z)^2} . \quad (1.12)$$

If we know the angular size of a source, we can measure its angular diameter distance and gain information on the Hubble rate. We show the three different distances for the current standard model in Figure 1.1.

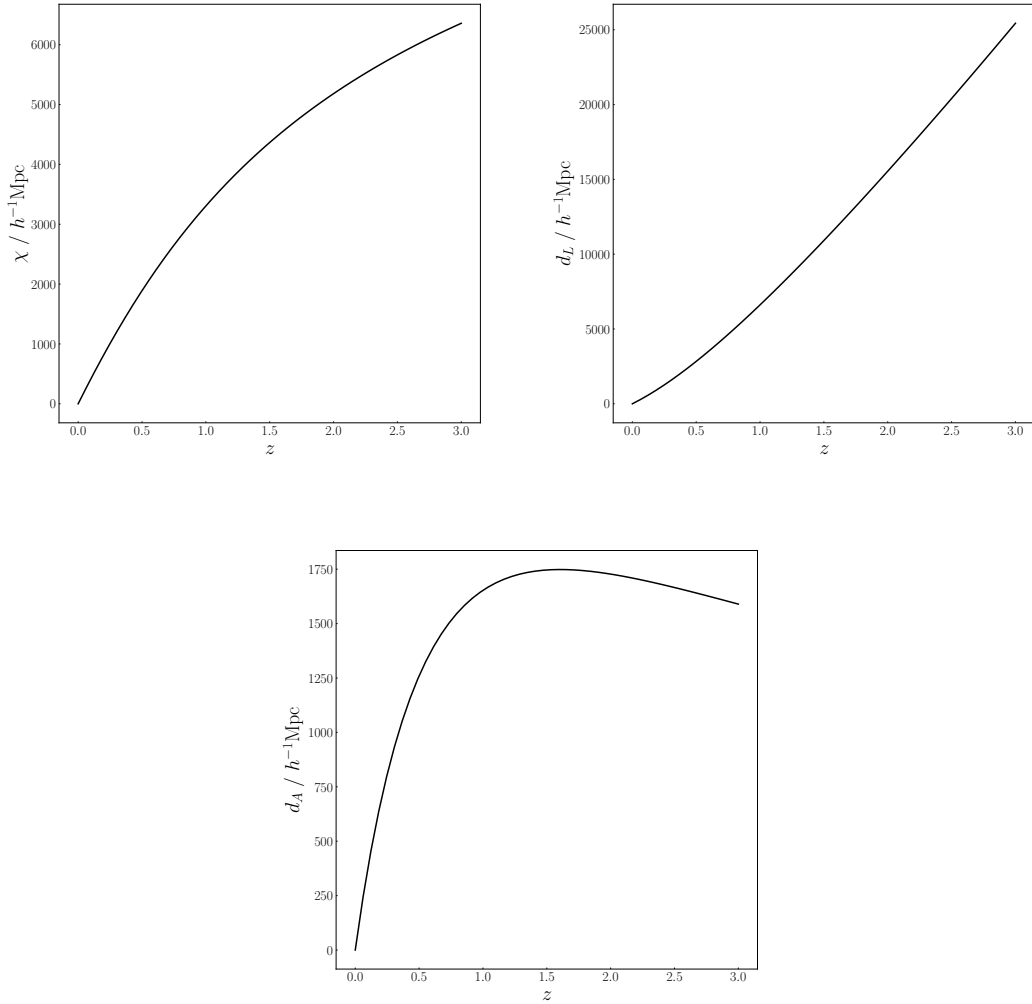


FIGURE 1.1: The comoving, luminosity and angular diameter distances as functions of redshift for the standard cosmological model, using the best-fit parameters of Planck 2018 [7]

1.2 Content of the Universe

Let us look at the inventory of the Universe. The observed light element abundances today, together with the predictions for light nucleosynthesis a few minutes after the start of the Universe – the so-called Big Bang Nucleosynthesis (BBN), and coupled with CMB observations, give a measure of the energy density of baryonic matter of about 5% of the total today. The radiation energy density (mainly photons but also light neutrinos¹) which dominated in the early Universe makes a very small contribution today. The energy density of cold dark matter contributes about 25%. The nature of dark matter is still unknown. It is widely thought to be a new fundamental particle which has negligible interactions with photons and with baryonic matter (and other standard fundamental particles). Experiments that attempt to make direct detections of dark matter particles have not yet been successful. The evidence for it is based on its gravitational effects on baryonic matter:

- Gravitational lensing can detect the dominant influence of the dark matter in the galaxies and clusters by measuring distortions of the lightrays from distant galaxies located behind lensing galaxies or clusters of galaxies.
- Spiral galaxies could not maintain the rotational velocities that are measured for their stars unless the mass within the galaxy is much higher than the total mass in baryonic matter (i.e., stars and gas).
- Without dark matter, galaxies would also need much longer than the current age of the universe to grow to what is observed today.

The remaining $\sim 70\%$ of the energy budget today is made up by a field which is called dark energy. In the General Relativity model of cosmology, dark energy must have strongly negative pressure, sufficient to cause the observed acceleration of the expansion of the Universe. The nature of dark energy is not known. Similar

¹ The small mass of neutrinos means that they are no longer ultra-relativistic (and therefore no longer part of ‘radiation’) in the late Universe. We will neglect their small effect on structure formation.

to dark matter, dark energy is indirectly detected by its gravitational effects. There has been no direct detection. The simplest model of dark energy is the cosmological constant Λ in the standard model of cosmology, which is called the Λ Cold Dark Matter (LCDM or Λ CDM) model.

Now we have to know how the energy densities change over time. For cold matter (dark matter and baryonic matter after recombination), the density scales as $1/\text{volume}$, since the number of particles in a comoving volume is conserved. Therefore

$$\rho_m = \frac{\rho_{m0}}{a^3} = \rho_{m0}(1+z)^3. \quad (1.13)$$

For black body radiation, the energy density dilutes by another factor of a , since the energy of photons scales with $1/\text{wavelength}$:

$$\rho_r = \frac{\rho_{r0}}{a^4} = \rho_{r0}(1+z)^4. \quad (1.14)$$

Since blackbody radiation obeys $\rho_r \propto T^4$, where T is the temperature, we also have

$$T = \frac{T_0}{a} = T_0(1+z). \quad (1.15)$$

Finally, dark energy in the form of the cosmological constant does not change with expansion:

$$\rho_\Lambda = \rho_{\Lambda0} = \frac{\Lambda}{8\pi G}. \quad (1.16)$$

The different scalings above mean that different components dominate the Universe at different times (see Figure 1.2). As we approach the Big bang, $a \rightarrow 0$, radiation dominates. During this period, baryons are coupled to photons and are effectively part of the radiation component. Going forward in time, it is clear that radiation density decreases faster than matter density. At redshift $z_{eq} \sim 3000$, the dark matter density is equal to that of radiation. For lower redshifts, equivalently

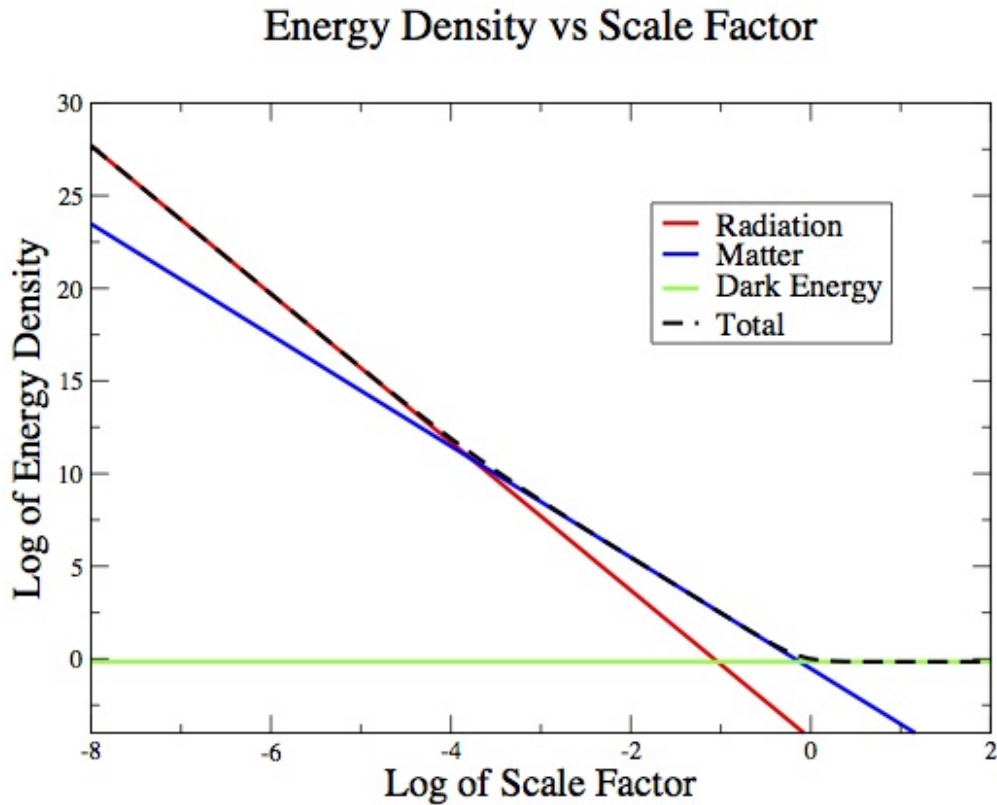


FIGURE 1.2: Evolution of the energy densities: radiation, matter and dark energy (Λ) against scale factor a (from [8]).

$a > a_{eq}$, non-relativistic matter dominates the Universe. During non-relativistic matter domination, at $z \sim 1000$, photons and baryons decouple, hydrogen atoms are formed (called ‘recombination’), the baryonic matter becomes effectively cold and the universe becomes transparent and radiation starts streaming freely. The dark energy density does not change with a , while radiation and matter densities continue to decrease. When $\rho_\Lambda = \rho_m$, which occurs at a low redshift, $z < 1$, the dark energy begins to dominate the Universe. (Note that the accelerating expansion starts before dark energy domination, because acceleration is sourced by the pressure as well as energy density of dark energy; see below.)

1.3 Background Dynamics

The background dynamics are governed by the Einstein field equations

$$R_{\mu\nu} - \frac{1}{2}Rg_{\mu\nu} = 8\pi GT_{\mu\nu}, \quad (1.17)$$

where $R_{\mu\nu}$ is the Ricci tensor of the metric $g_{\mu\nu}$, which is the FLRW metric (1.8), and $R = R^\mu_\mu$ is the Ricci scalar. On the right is the energy-momentum tensor,

$$T_{\mu\nu} = (\rho + P)u_\mu u_\nu + P g_{\mu\nu}, \quad (1.18)$$

where u^μ is the four-velocity of the matter-energy, which has energy density

$$\rho = \sum_i \rho_i = \rho_r + \rho_m + \rho_\Lambda, \quad (1.19)$$

and P is the total pressure. In FLRW spacetime, the four-velocities of all components are equal:

$$u^\mu = u_r^\mu = u_m^\mu = \frac{1}{a}\delta_0^\mu. \quad (1.20)$$

(Note that the cosmological constant does not have a four-velocity.) The pressure for each component can be written in terms of the equation of state parameter ω_i :

$$P_i = \omega_i \rho_i, \quad \text{where} \quad \omega_r = \frac{1}{3}, \quad \omega_m = 0, \quad \omega_\Lambda = -1. \quad (1.21)$$

The Einstein equations (1.17) enforce the energy-momentum conservation equation

$$\nabla_\nu T^{\mu\nu} = 0, \quad (1.22)$$

which can be split into energy and momentum conservation equations:

$$u_\mu(\nabla_\nu T^{\mu\nu}) = 0 \Rightarrow \rho' + 3\mathcal{H}(\rho + P) = 0, \quad (1.23)$$

$$(u_\mu u_\alpha + g_{\mu\alpha})(\nabla_\nu T^{\mu\nu}) = 0 \Rightarrow 0 = 0. \quad (1.24)$$

Assuming no interaction amongst the components, each one separately obeys

$$\nabla_\nu T_i^{\mu\nu} = 0. \quad (1.25)$$

Then for each component, energy conservation (1.23) leads to the scaling relations (1.13)–(1.16), using (1.21). Momentum conservation holds automatically in FLRW spacetime since any nonzero momentum is forbidden by the Cosmological Principle.

Einstein's equations for FLRW reduce to two independent equations:

$$H^2 = \frac{8\pi G}{3}\rho = \frac{8\pi G}{3}(\rho_m + \rho_r) + \frac{\Lambda}{3}, \quad (1.26)$$

$$\mathcal{H}^2 = \frac{8\pi G}{3}\rho a^2, \quad (1.27)$$

$$\frac{\ddot{a}}{a} = -\frac{4\pi G}{3}(\rho + 3P) = -\frac{4\pi G}{3}(\rho_m + 2\rho_r) + \frac{\Lambda}{3}, \quad (1.28)$$

$$\mathcal{H}' = -\frac{4\pi G}{3}(\rho + 3P)a^2. \quad (1.29)$$

(1.26) and (1.27) are the Friedmann equation in proper vs conformal times and similarly for the acceleration equation. This equation shows explicitly how Λ contributes to acceleration, $\ddot{a} > 0$, while matter and radiation always contribute only to deceleration, $\ddot{a} < 0$.

The dimensionless density parameters are defined by

$$\Omega_i = \frac{\rho_i}{\rho_{crit}} = \frac{8\pi G a^2 \rho_i}{3\mathcal{H}^2}, \quad (1.30)$$

which means the Friedmann equation becomes:

$$\sum_i \Omega_i = \Omega_r + \Omega_m + \Omega_\Lambda = 1. \quad (1.31)$$

The evolution of these is shown in Figure 1.3 , using the CLASS package [9, 10]. In this Figure we also show three critical redshifts in the Planck 2018 best-fit Λ CDM model [7]. In particular:

$$z_{eq} = 3406.9. \quad (1.32)$$

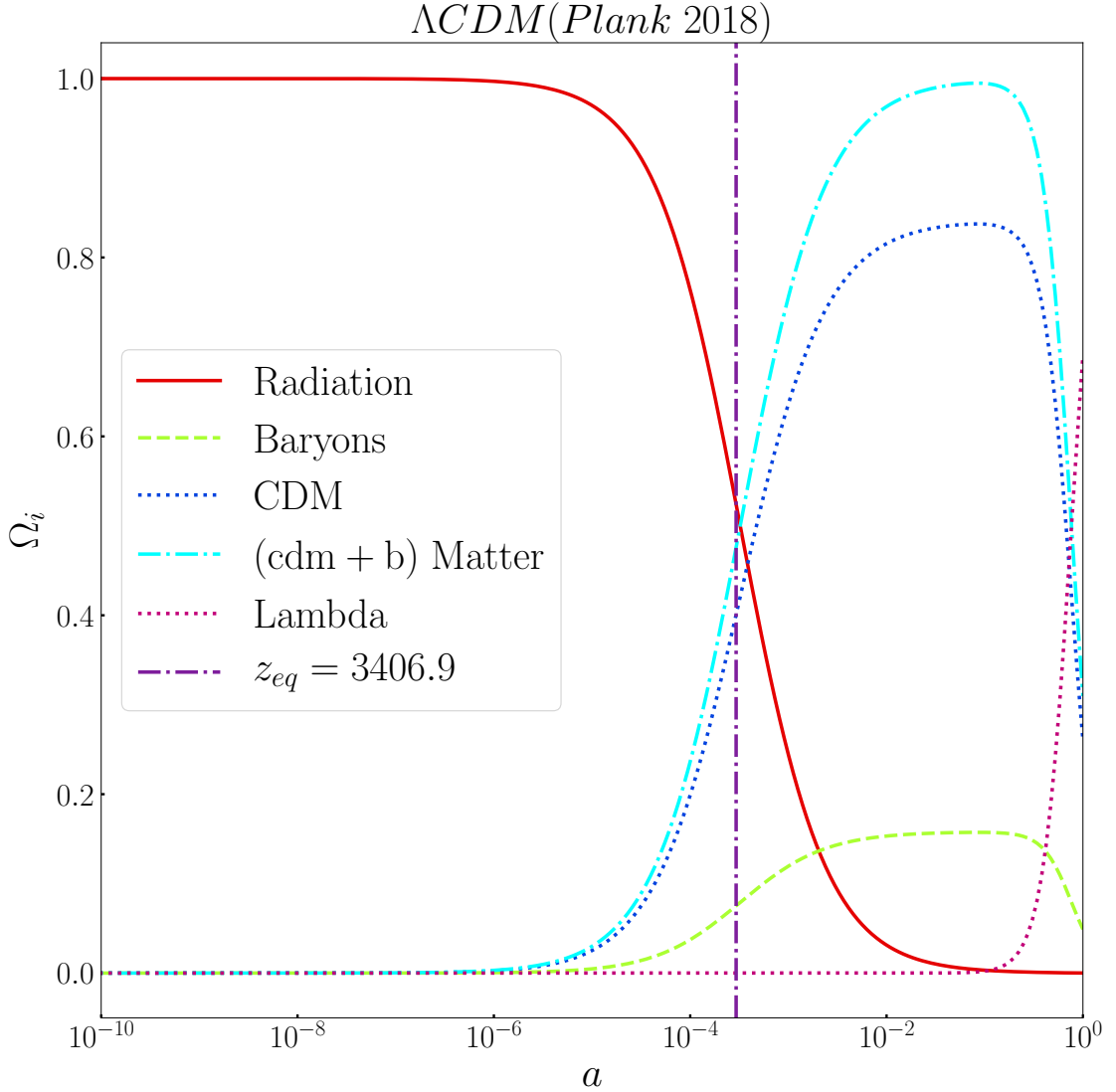


FIGURE 1.3: Evolution of dimensionless densities Ω_i in Λ CDM with Planck 2018 best-fit parameters. Critical redshift of z_{eq} (matter–radiation equality) is also shown in dashed dotted vertical line.

For constant ω we have exact solutions:

$$H = \frac{2}{3(1+\omega)t}, \quad \mathcal{H} = \frac{2}{(1+3\omega)\eta}, \quad (1.33)$$

$$a(t) \propto t^{2/3(1+\omega)}, \quad a(\eta) \propto \eta^{2/(1+3\omega)}. \quad (1.34)$$

The proper time solutions hold only for $\omega \neq -1$. When $\omega = -1$, we have

$$H = H_0, \quad \mathcal{H} = -\frac{1}{\eta}, \quad (1.35)$$

$$a(t) \propto e^{H_0 t}, \quad a(\eta) \propto \eta^{-1}. \quad (1.36)$$

The $\omega = -1$ case applies approximately to Inflation in the very early Universe (before the radiation era) and also in future Universe when $\Omega_\Lambda \rightarrow 1$.

For the radiation-dominated era, we have $\omega = 1/3$ and

$$H(z) = H_0 \sqrt{\Omega_{r0}} (1+z)^2. \quad (1.37)$$

In the matter-dominated universe, known as the Einstein de Sitter (EdS) model, we have $\omega = 0$ and

$$H(z) = H_0 \sqrt{\Omega_{m0}} (1+z)^{3/2}. \quad (1.38)$$

After recombination, we need to include the effect of dark energy – this is the Λ CDM model at late times, relevant for structure formation:

$$H(z) = H_0 \sqrt{\Omega_{m0} (1+z)^3 + 1 - \Omega_{m0}}. \quad (1.39)$$

Chapter 2

Cosmological Perturbations for Large-Scale Structure

We give a brief review of cosmological perturbation theory that is needed to analyse large-scale structure formation – i.e., the growth from small primordial fluctuations of galaxies. This review is based on [2–6, 11–14].

Cosmological perturbation theory (at linear, or first, order) considers small fluctuations around the FLRW background described in Chapter 1. In the standard model of cosmology, the origin of these fluctuations is inflation: a brief period of very high energy accelerated expansion, starting almost immediately after the origin of the Universe. The field or fields that drive inflation also generate quantum fluctuations on very small scales – which are stretched by the rapid acceleration to become classical fluctuations in the curvature and energy densities of the Universe. These classical fluctuations are the seeds for the temperature fluctuations in the CMB, that are seen in the sky maps produced by telescopes such as Planck. In this thesis we do not consider the CMB fluctuations, but focus on the later fluctuations in the cold matter. These matter perturbations, seeded by inflation, are the origin of the large-scale structure, i.e., the galaxies and their distribution, in the Universe.

Linear perturbations of an FLRW background are based on metric and energy-momentum perturbations:

$$g_{\mu\nu}(\eta, \mathbf{x}) = \bar{g}_{\mu\nu}(\eta) + \delta g_{\mu\nu}(\eta, \mathbf{x}), \quad T_{\mu\nu}(\eta, \mathbf{x}) = \bar{T}_{\mu\nu}(\eta) + \delta T_{\mu\nu}(\eta, \mathbf{x}). \quad (2.1)$$

Here $\bar{g}_{\mu\nu}(\eta)$ and $\bar{T}_{\mu\nu}(\eta)$ represent the FLRW background components and $\delta g_{\mu\nu}(\eta, \mathbf{x})$ and $\delta T_{\mu\nu}(\eta, \mathbf{x})$ are the linear perturbations. In Newtonian gauge we can write the perturbed metric as

$$ds^2 = a(\eta)^2 \{ - [1 + 2\Phi(\eta, \mathbf{x})] d\eta^2 + [1 - 2\Phi(\eta, \mathbf{x})] \delta_{ij} dx^i dx^j \}, \quad (2.2)$$

where Φ is the gravitational potential that describes time and spatial curvature perturbations. In general the spatial and time potentials are unequal, but in the late Universe these potentials are equal to a very good approximation.

The energy-momentum perturbations require firstly the perturbed density and pressure:

$$\rho(\eta, \mathbf{x}) = \bar{\rho}(\eta) + \delta\rho(\eta, \mathbf{x}) = \bar{\rho}(\eta) [1 + \delta(\eta, \mathbf{x})], \quad P = \bar{P}(\eta) + \delta P(\eta, \mathbf{x}), \quad (2.3)$$

where the density contrast itself is defined by $\delta = \delta\rho/\bar{\rho}$. Secondly, we need the perturbed 4-velocity of matter:

$$u^\mu = \frac{dx^\mu}{d\tau} = \bar{u}^\mu + \delta u^\mu.$$

Using the general relation in any spacetime:

$$g_{\mu\nu} u^\mu u^\nu = \frac{g_{\mu\nu} dx^\mu dx^\nu}{d\tau^2} = -1, \quad (2.4)$$

we can show that

$$2\bar{g}_{\mu\nu} \delta u^\mu \bar{u}^\nu + \delta g_{\mu\nu} \bar{u}^\mu \bar{u}^\nu = 0. \quad (2.5)$$

Now we can write

$$u^\mu = \frac{1}{a} (1 + a\delta u^0, v^i), \quad (2.6)$$

where we wrote δu^i as v^i/a . Since we are interested only in scalar perturbations for large-scale structure, the so-called peculiar velocity v^i is irrotational, i.e. it can be written as the gradient of a scalar velocity potential V :

$$v_i = \partial_i V. \quad (2.7)$$

Finally, from (2.5), we find δu^0 and v^i :

$$u^\mu = \bar{u}^\mu + \delta u^\mu = \frac{1}{a} (1 - \Phi, \partial^i V). \quad (2.8)$$

2.1 Perturbation of Conservation Equations

The adiabatic sound speed is given by

$$c_s^2 = \frac{\partial \bar{P}}{\partial \bar{\rho}} = \frac{\bar{P}'}{\bar{\rho}'} . \quad (2.9)$$

Then it follows that

$$\omega' = 3\mathcal{H}(\omega - c_s^2)(1 + \omega) , \quad (2.10)$$

and

$$\delta P = c_s^2 \delta \rho . \quad (2.11)$$

From (2.1) we find the perturbed energy-momentum tensor as:

$$\begin{aligned} \delta T_0^0 &= -\delta \rho , \\ \delta T_i^0 &= (\bar{\rho} + \bar{P}) \partial_i V , \\ \delta T_j^i &= \delta P \delta_j^i . \end{aligned} \quad (2.12)$$

where

$$\delta T_i^0 = q_i = (\bar{\rho} + \bar{P}) \partial_i V , \quad (2.13)$$

is the momentum density of the moving fluid q_i . The energy-momentum conservation equation in a perturbed FLRW model is

$$\bar{\nabla}_\mu \bar{T}_\nu^\mu + \delta(\nabla_\mu T_\nu^\mu) = 0 . \quad (2.14)$$

In order to compute this equation, we need the perturbed Christoffel symbols:

$$\Gamma_{00}^0 = \mathcal{H} + \Phi' \quad (2.15)$$

$$\Gamma_{00}^i = \partial^i \Phi \quad (2.16)$$

$$\Gamma_{0i}^0 = \partial_i \Phi \quad (2.17)$$

$$\Gamma_{0j}^i = (\mathcal{H} - \Phi') \delta_j^i \quad (2.18)$$

$$\Gamma_{ij}^0 = \mathcal{H} - [\Phi' + 4\mathcal{H}\Phi] \delta_{ij} \quad (2.19)$$

$$\Gamma_{0j}^i = \delta_{jk} \partial^k \Phi - \delta_j^i \partial_k \Phi - \delta_k^i \partial_j \Phi. \quad (2.20)$$

Then we recover the background energy conservation equation

$$\bar{\rho}' + 3\mathcal{H}(\bar{\rho} + \bar{P}) = 0, \quad (2.21)$$

and the trivial background momentum conservation. In addition, we get the perturbation of conserved energy and momentum, $\nu = 0$ and $\nu = i$ respectively, as:

$$\delta\rho' + 3\mathcal{H}(\delta\rho + \delta P) = (\bar{\rho} + \bar{P})(3\Phi' - \nabla^2 V), \quad (2.22)$$

$$[(\bar{\rho} + \bar{P})V]' + \delta P = -(\bar{\rho} + \bar{P})(\Phi + 4\mathcal{H}V). \quad (2.23)$$

We can rewrite these energy and momentum conservation equations as:

$$\delta' + 3(c_s^2 - \omega)\mathcal{H}\delta = (1 + \omega)(3\Phi' - \nabla^2 V), \quad (2.24)$$

$$V' + (1 - 3c_s^2)\mathcal{H}V = -\Phi - \frac{c_s^2}{1 + \omega}\delta. \quad (2.25)$$

For a late-time Λ CDM model, $c_s = 0 = \omega$ and we get

$$\delta'_m = 3\Phi' - \nabla^2 V_m, \quad (2.26)$$

$$V'_m + \mathcal{H}V_m = -\Phi, \quad (2.27)$$

where δ_m is the matter density contrast and V_m is the matter velocity potential. We define the *comoving matter density contrast* Δ_m as the density contrast that

is measured by observers moving with the matter. It is given by

$$\Delta_m = \delta_m + \frac{\bar{\rho}'_m}{\bar{\rho}_m} V_m = \delta_m - 3\mathcal{H}V_m. \quad (2.28)$$

The energy conservation equation for the comoving matter density contrast is then

$$\Delta'_m = -\nabla^2 V_m, \quad (2.29)$$

after using (2.27).

2.2 Perturbation of Einstein Field Equations

The perturbations of Einstein's equations,

$$\delta G_{\mu\nu} = 8\pi G \delta T_{\mu\nu} \quad (2.30)$$

are determined from perturbed Ricci tensor and scalar,

$$\delta G_{\mu\nu} = \delta R_{\mu\nu} - \frac{1}{2}(\bar{g}_{\mu\nu}\delta R + \bar{R}\delta g_{\mu\nu}), \quad (2.31)$$

together with the perturbed energy-momentum tensor. The perturbed Ricci tensor components are:

$$\begin{aligned} \delta R_{00} &= 3(\Phi'' + 2\mathcal{H}\Phi') + \nabla^2\Phi \\ \delta R_{0i} &= 2\partial_i(\Phi' + \mathcal{H}\Phi) \\ \delta R_{ij} &= [\nabla^2\Phi - \Phi'' - 6\mathcal{H}\Phi' - 4(\mathcal{H}' + 2\mathcal{H}^2)\Phi]\delta_{ij} \end{aligned} \quad (2.32)$$

Then we can calculate the perturbed Ricci Scalar, given that:

$$\delta R = \delta R_{\mu\nu}\bar{g}^{\mu\nu} + \bar{R}_{\mu\nu}\delta g^{\mu\nu} \quad (2.33)$$

This reduces to

$$\delta R = 2a^{-2}[\nabla^2\Phi - 3\Phi'' - 12\mathcal{H}\Phi' - 6(\mathcal{H}' + \mathcal{H}^2)\Phi] \quad (2.34)$$

We have to use (2.32), (2.31) and (2.34) to get Perturbed Einstein tensor:

$$\begin{aligned} \delta G_{00} &= 2\nabla^2\Phi - 6\mathcal{H}\Phi' \\ \delta G_{0i} &= 2\partial_i(\Phi' + \mathcal{H}\Phi) \\ \delta G_{ij} &= [2\Phi'' + 6\mathcal{H}\Phi' + 4(2\mathcal{H}' + \mathcal{H}^2)\Phi]\delta_{ij}. \end{aligned} \quad (2.35)$$

Using the two results for $\delta G_{\mu\nu}$ (2.35) and $\delta T_{\mu\nu}$ (2.12) shows that the perturbed Einstein Field equations are

$$\begin{aligned} (00) : \quad & \nabla^2 \Phi = 4\pi G a^2 \delta \rho + 3\mathcal{H}(\Phi' + \mathcal{H}\Phi) \\ (0i) : \quad & \Phi' + \mathcal{H}\Phi = -4\pi G a^2 \rho(1 + \omega)V \\ (ij) : \quad & \Phi'' + 3\mathcal{H}\Phi' + [4\mathcal{H}' + (2 + 3\omega)\mathcal{H}^2]\Phi = 4\pi G a^2 \delta P. \end{aligned} \quad (2.36)$$

The Poisson equation (00) determines the density contrast δ from the potential Φ , while the momentum constraint equation (0i) determines the velocity potential V

$$\nabla^2 \Phi = 4\pi G a^2 \bar{\rho} \delta + 3\mathcal{H}(\Phi' + \mathcal{H}\Phi) \quad (2.37)$$

$$\Phi' + \mathcal{H}\Phi = -4\pi G a^2 \rho(1 + \omega)V \quad (2.38)$$

The potential itself is determined by the Bardeen equation (ij), where δP is expressed in terms of Φ by using (2.11) and the Poisson equation (2.37):

$$\Phi'' + 3(1 + c_s^2)\mathcal{H}\Phi' + 3(c_s^2 - \omega)\mathcal{H}^2\Phi = c_s^2 \nabla^2 \Phi \quad (2.39)$$

2.3 Evolution of Perturbations

Using the Bardeen equation (2.39), we can find the potential in the radiation-dominated, matter-dominated and late-time Λ CDM eras:

- *Radiation era:*

In the radiation dominated era of the universe, (2.39) in Fourier space becomes

$$\Phi'' + \frac{4}{\eta}\Phi' + \frac{k^2}{3}\Phi = 0, \quad (2.40)$$

which has growing-mode (or regular) solution

$$\Phi(\eta, \mathbf{k}) = A_{\mathbf{k}} \frac{j_1(x)}{x}, \quad x = c_s k \eta = \frac{k \eta}{\sqrt{3}}. \quad (2.41)$$

$x \ll 1$ means that $k \ll \mathcal{H}$, corresponding to super-Hubble scales, with $j_1(x) \rightarrow x/3$. This implies that the potential evolution in radiation-dominated era become constant on super-Hubble scales. On sub-Hubble scales, $k \gg \mathcal{H}$ and $x \gg 1$, the solution is oscillating, with decaying envelope x^{-2} :

$$\Phi(\eta, \mathbf{k}) \rightarrow \frac{A_{\mathbf{k}}}{3} \quad k \ll \mathcal{H} \quad (2.42)$$

$$\Phi(\eta, \mathbf{k}) \rightarrow -3A_{\mathbf{k}} \frac{\cos(k\eta/\sqrt{3})}{k^2 \eta^2} \quad k \gg \mathcal{H} \quad (2.43)$$

- *Matter era (Einstein de Sitter model):*

In the matter dominated era of the universe, (2.39) in Fourier space becomes

$$\Phi'' + \frac{6}{\eta}\Phi' = 0, \quad (2.44)$$

which has growing-mode (or regular) solution

$$\Phi(\eta, \mathbf{k}) = B_{\mathbf{k}}. \quad (2.45)$$

In other words, the potential is constant in time on all scales.

- Late-time Λ CDM era:

From Bardeen equation we have:

$$\Phi'' + 3\mathcal{H}\Phi' + 3\Lambda a^2\Phi = 0 \quad (2.46)$$

We can rewrite the equation in terms of the *growth suppression factor* g , where

$$\Phi(\eta, \mathbf{k}) = g(\eta) \Phi_0(\mathbf{k}) \quad (2.47)$$

where Φ_0 is the potential today. Then

$$g'' + 3\mathcal{H}g' + 3\Lambda a^2g = 0. \quad (2.48)$$

Since $\Lambda > 0$ this means that dark energy contributes to $g' < 0$ and the gravitational potential is suppressed relative to the matter era. This is shown in Figure 2.1.

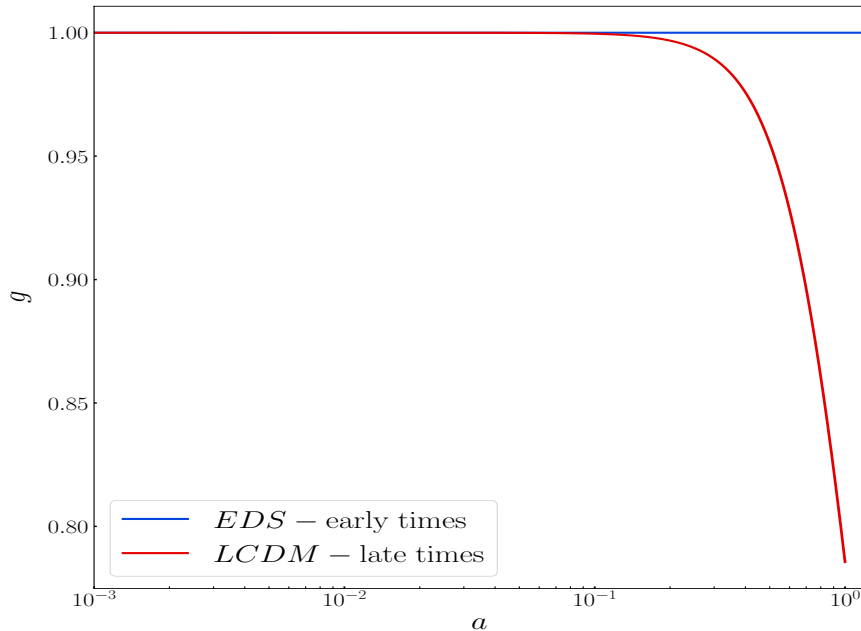


FIGURE 2.1: Growth suppression factor for Λ CDM and EdS.

In the late-time Λ CDM era, the Poisson equation is simplified when we use the comoving matter density contrast:

$$\nabla^2 \Phi = \frac{3}{2} \Omega_m \mathcal{H}^2 \Delta_m, \quad (2.49)$$

so that in Fourier space

$$\Delta_m(\eta, \mathbf{k}) = -\frac{2}{3\Omega_m(\eta)\mathcal{H}^2(\eta)} k^2 \Phi(\eta, \mathbf{k}) \quad (2.50)$$

Defining the *growth factor* D by

$$\Delta_m(\eta, \mathbf{k}) = D(\eta) \Delta_{m0}(\mathbf{k}), \quad (2.51)$$

we find the late-time Λ CDM evolution equation for density contrast:

$$D'' + \mathcal{H}D' - \frac{3}{2} \Omega_m \mathcal{H}^2 D = 0. \quad (2.52)$$

Note that $g = D/a$. In matter domination, $D = a$ and dark energy will reduce this growth. Now the dimensionless matter growth rate f is given by:

$$f = \frac{d \ln D}{d \ln a}. \quad (2.53)$$

In EdS, $f = 1$ but in LCDM it drops below 1. The evolution equation (2.52) becomes

$$\frac{df}{d \ln a} + \frac{1}{2}(4 - 3\Omega_m)f + f^2 = \frac{3}{2}\Omega_m, \quad (2.54)$$

with initial condition $f_{in} = 1$ where $10^{-3} \lesssim a_{in} \lesssim 10$, i.e. in matter domination, after recombination. See Figure 2.2 for the solution. A very good approximation to the solution is

$$f(z) = [\Omega_m(z)]^\gamma, \quad \gamma = 0.545 \quad (2.55)$$

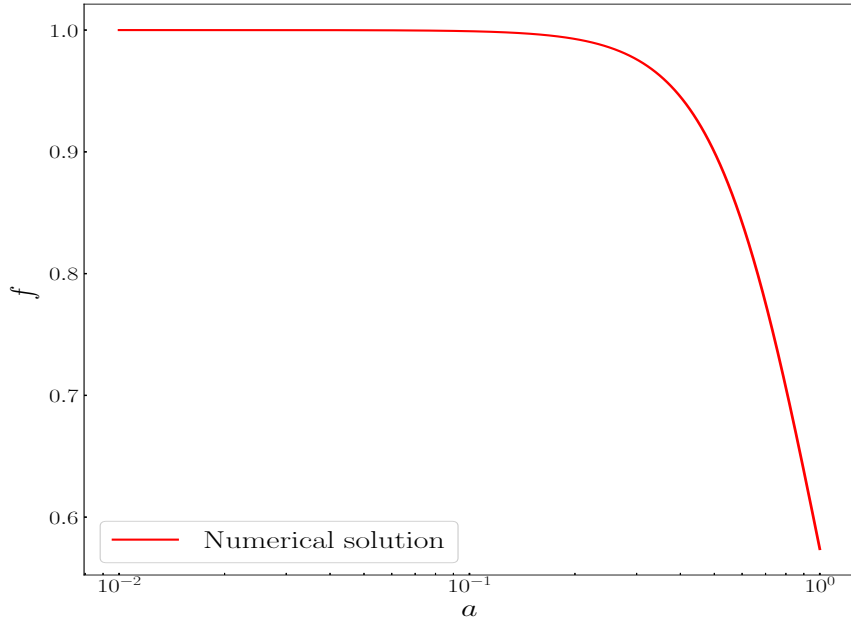


FIGURE 2.2: Evolution of LCDM growth rate.

It is clear that $k = \mathcal{H}$ is a critical scale which divides sub-Hubble and super-Hubble modes that can behave quite differently in the radiation era. Sub-Hubble modes are suppressed during radiation domination, but not during matter domination. The wavelength

$$\lambda = \frac{2\pi a}{k} \quad (2.56)$$

of all modes grows with expansion. Each classical mode originates with wavelength greater than the Hubble radius $1/H_{\text{inf}}$ during inflation. After inflation, H grows while the comoving wavenumber of the mode k is constant. This means that the wavelength of all modes eventually become smaller than the Hubble radius (until the universe starts to accelerate again):

$$\lambda < H^{-1} \quad \text{equivalent to} \quad k > \mathcal{H} \quad (2.57)$$

Modes that become sub-Hubble during the radiation era are suppressed in amplitude relative to modes that become sub-Hubble during matter domination. This means that there is a critical comoving wavenumber, defined by the conformal

Hubble rate at the transition from radiation domination to matter domination. The transition occurs at *matter-radiation equality*, where

$$\rho_m(z_{\text{eq}}) = \rho_r(z_{\text{eq}}) \Rightarrow 1 + z_{\text{eq}} = \frac{\Omega_{m,0}}{\Omega_{r,0}} \quad (2.58)$$

$$\Rightarrow \mathcal{H}_{\text{eq}}^2 = 2 \frac{\Omega_{m,0}^2}{\Omega_{r,0}} H_0^2 \quad (2.59)$$

This implies that the critical scale is:

$$k_{\text{eq}} = \mathcal{H}_{\text{eq}} = \sqrt{\frac{2}{\Omega_{r,0}}} \Omega_{m,0} H_0 \quad (2.60)$$

Modes with $k > k_{\text{eq}}$ enter the Hubble radius during radiation domination and are therefore suppressed relative to those with $k < k_{\text{eq}}$, which enter during matter domination. This applies to the potential Φ and then, using the Poisson equation, to the comoving density contrast Δ_m in late LCDM.

Note that on super-Hubble scales, the (constant) amplitude of Φ in the radiation and matter eras are different:

$$\Phi_{\text{mat}}(k \ll \mathcal{H}) = \frac{9}{10} \Phi_{\text{rad}}(k \ll \mathcal{H}). \quad (2.61)$$

This follows from using the comoving curvature perturbation

$$\zeta = \Phi - \mathcal{H}V = \frac{2}{3(1+\omega)\mathcal{H}}(\Phi' + \mathcal{H}\Phi) \quad (2.62)$$

where the second equality follows from momentum constraint (2.37). Then we find that

$$\zeta' = \frac{2}{3(1+\omega)\mathcal{H}} c_s^2 \nabla^2 \Phi, \quad (2.63)$$

so that

$$\zeta' = 0 \quad \text{for } k \ll \mathcal{H}. \quad (2.64)$$

It follows that the *primordial* curvature perturbation, i.e. during Inflation, is the same as the curvature perturbation on super-Hubble scales in the radiation, then matter and then dark energy eras. We have

$$\zeta = \frac{(5 + 3\omega)}{3(1 + \omega)} \Phi \quad \text{for } k \ll \mathcal{H}. \quad (2.65)$$

Since

$$\Phi_{\text{rad}} = \frac{2}{3}\zeta \quad \text{for } k \ll \mathcal{H} \quad (2.66)$$

$$\Phi_{\text{mat}} = \frac{3}{5}\zeta \quad \text{for } k \ll \mathcal{H}, \quad (2.67)$$

we arrive at (2.61).

2.4 Power Spectrum

The power spectrum of the primordial curvature perturbation is

$$P_\zeta(k) = |\zeta(\mathbf{k})|^2 = \frac{A_s}{k_*^3} \left(\frac{k}{k_*} \right)^{n_s - 1}, \quad (2.68)$$

where $A_s = 2.14 \times 10^9$ is the amplitude, $n_s = 0.9603$ is the scalar spectral index and the reference scale is $k_* = 0.05 \text{ Mpc}^{-1}$ [7].

The suppression of potential modes during the radiation dominated era can be expressed in terms of a transfer function

$$\Phi(\eta, \mathbf{k}) \propto g(\eta) T(\eta, k) \zeta(\mathbf{k}), \quad (2.69)$$

where we have omitted a numerical constant. The suppression of matter density contrast modes follows from (2.70) as

$$\Delta_m(\eta, \mathbf{k}) \propto -\frac{D(\eta)}{\Omega_m(\eta) \mathcal{H}^2(\eta)} k^2 T(\eta, k) \zeta(\mathbf{k}), \quad (2.70)$$

where

$$T \rightarrow 1 \quad \text{for} \quad k \ll \mathcal{H} \quad (2.71)$$

$$T \rightarrow 0 \quad \text{for} \quad k \gg \mathcal{H} \quad (2.72)$$

The form of T needs to be computed numerically: this is illustrated in Figure 2.3

The matter power spectrum is

$$P_m(\eta, k) = |\Delta_m(\eta, \mathbf{k})|^2 \propto k^4 T^2(\eta, k) P_\zeta(\mathbf{k}). \quad (2.73)$$

Figure 2.4 shows how the matter power spectrum behaves with wavenumber at two redshifts. P_m reduces with z , reflecting the growth of density contrast with time. The turning point at k_{eq} is shown, together with the scale $k_{\mathcal{H}_0} = H_0$. The Hubble scale today gives an order of magnitude of the maximal length that

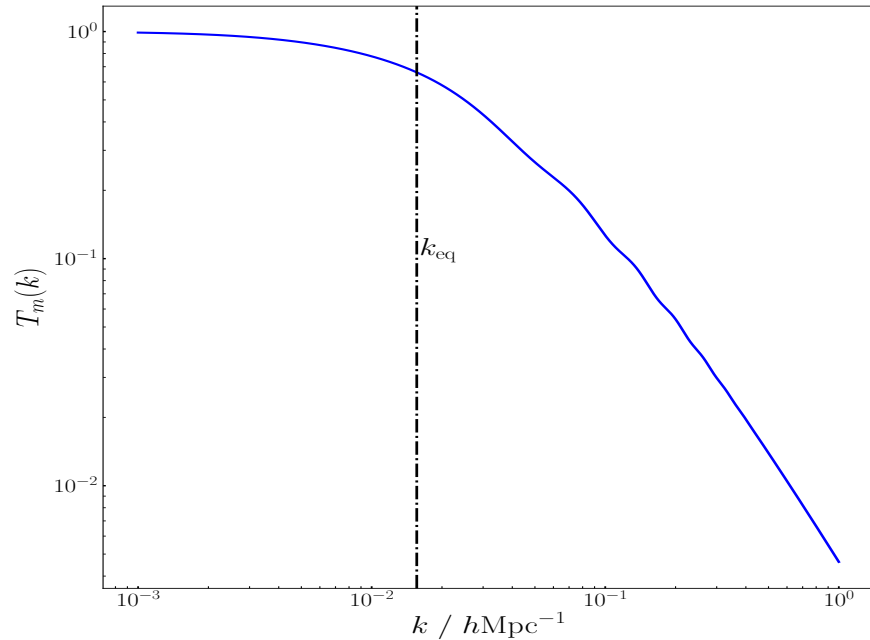


FIGURE 2.3: The matter transfer function at redshift $z = 0.1$ computed using CLASS [9]. The black dashed line represents k at equality.

could be measured in principle. Figure 2.5 shows the dimensionless matter power spectrum $k^3 P_m$, which tends to a constant on small linear scales.

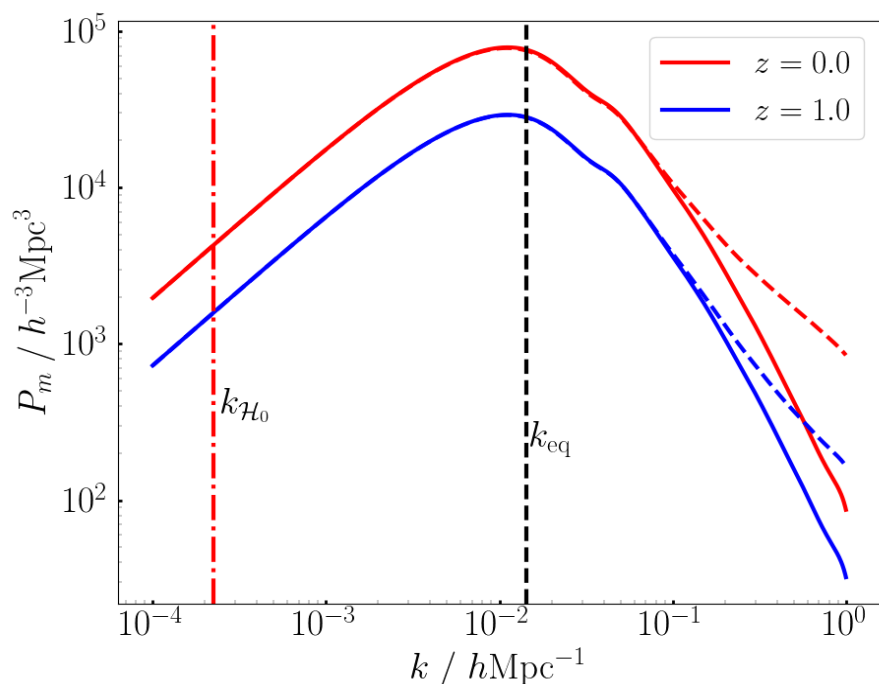


FIGURE 2.4: The matter power spectrum P_m computed using CLASS. The solid lines are the linear power spectrum while the dashed lines that are shown on small scales (large k) are the non-linear power implemented by the HALOFIT option in CLASS. The dash dotted vertical line k_{H_0} (red) and dashed line k_{eq} (black) are also shown.

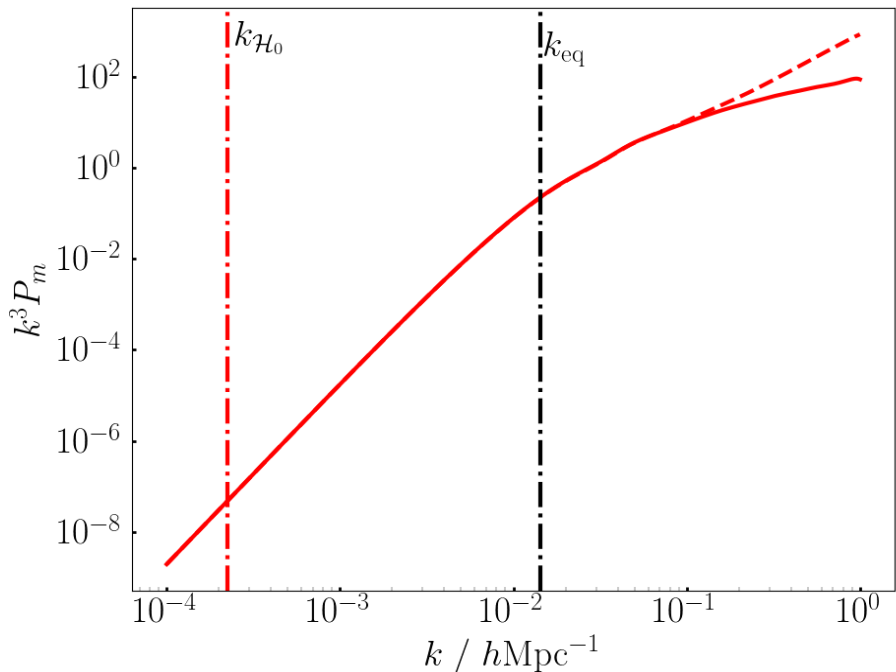


FIGURE 2.5: Linear (solid) and non-linear (dotted line) model of the dimensionless matter power spectrum at $z = 0$.

2.5 Galaxy and HI Intensity Mapping Surveys

Galaxy surveys involve counting galaxies and measuring their redshift and angular position. By definition they have high angular accuracy. Their ‘radial’ or redshift accuracy depends on whether they are spectroscopic (high accuracy) or photometric (lower accuracy). The galaxy number density contrast is

$$\delta_g = \frac{\delta n_g}{\bar{n}_g} = \frac{n_g - \bar{n}_g}{\bar{n}_g}. \quad (2.74)$$

On linear scales, we can relate this to the matter density contrast via the galaxy bias b where:

$$\delta_g(z, \mathbf{k}) = b(z)\delta_m(z, \mathbf{k}). \quad (2.75)$$

The key point is that b is independent of k . Note that we can rewrite this relation using the comoving density contrasts Δ_g, Δ_m , but these are well approximated by δ_g, δ_m on small scales.

In this thesis we are concerned with a different kind of survey, known as a neutral hydrogen (HI) intensity mapping survey. HI atoms emit radio photons of rest-frame wavelength 21 cm, which redshift as

$$\lambda(z) = \lambda_{21}(1 + z) = 21(1 + z) \text{ cm.} \quad (2.76)$$

After reionization $z \lesssim 6$, nearly all HI is in galaxies. But an HI intensity map does not detect individual HI-emitting galaxies. Instead, the survey attempts to measure the total (integrated) emission of 21 cm radiation at a chosen redshift. The intensity is given by the brightness temperature T_{HI} of the 21 cm radiation. At the chosen z , the results is a brightness temperature map of the area of the covered. The redshift accuracy of HI intensity mapping surveys planned for the near future is very high. But the angular resolution is poor, since individual emitters are not detected.

Fluctuations δT_{HI} around the average \bar{T}_{HI} then give a measure of the underlying density contrast of HI galaxies. They are defined as

$$\delta_{\text{HI}} = \frac{\delta T_{\text{HI}}}{\bar{T}_{\text{HI}}} = \frac{T_{\text{HI}} - \bar{T}_{\text{HI}}}{\bar{T}_{\text{HI}}}, \quad (2.77)$$

where \bar{T}_{HI} is HI background temperature. Similar to galaxy bias, we can define the HI bias

$$\delta_{\text{HI}}(z, \mathbf{k}) = b_{\text{HI}}(z) \delta_m(z, \mathbf{k}). \quad (2.78)$$

Then the HI power spectrum is related to the matter power spectrum by

$$P_{\text{HI}}(z, k) = b_{\text{HI}}^2(z) P_m(z, k). \quad (2.79)$$

We will use the model of [15] for the average brightness temperature:

$$\bar{T}_{\text{HI}} = 5.5919 \times 10^{-2} + 2.3242 \times 10^{-1} z - 2.4136 \times 10^{-2} z^2 \text{ mK}. \quad (2.80)$$

For the HI bias we use the model of [16]:

$$b_{\text{HI}}(z) = 0.754 + 0.0877z + 0.0607z^2 - 0.00274z^3, \quad (2.81)$$

(For more details, see [15, 17]). We showed the results of (2.80) and (2.81) against redshift z on Figure 2.6 and 2.7 below.

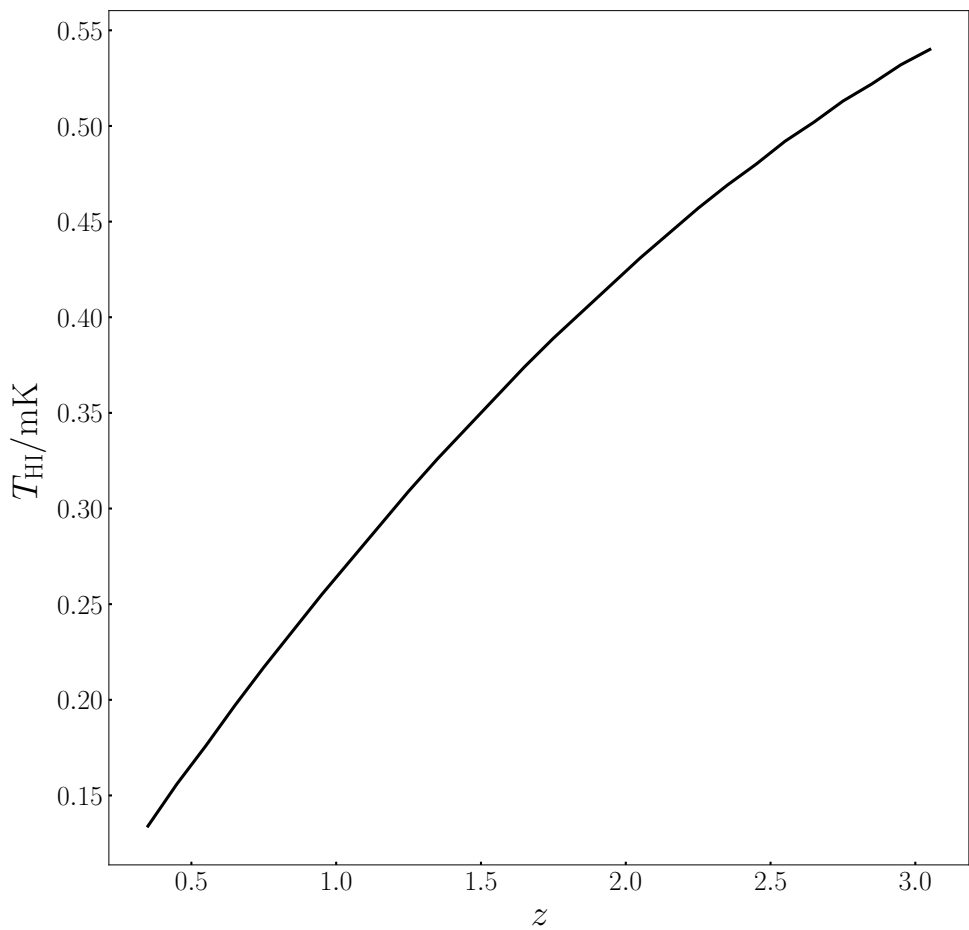


FIGURE 2.6: The average brightness temperature against z

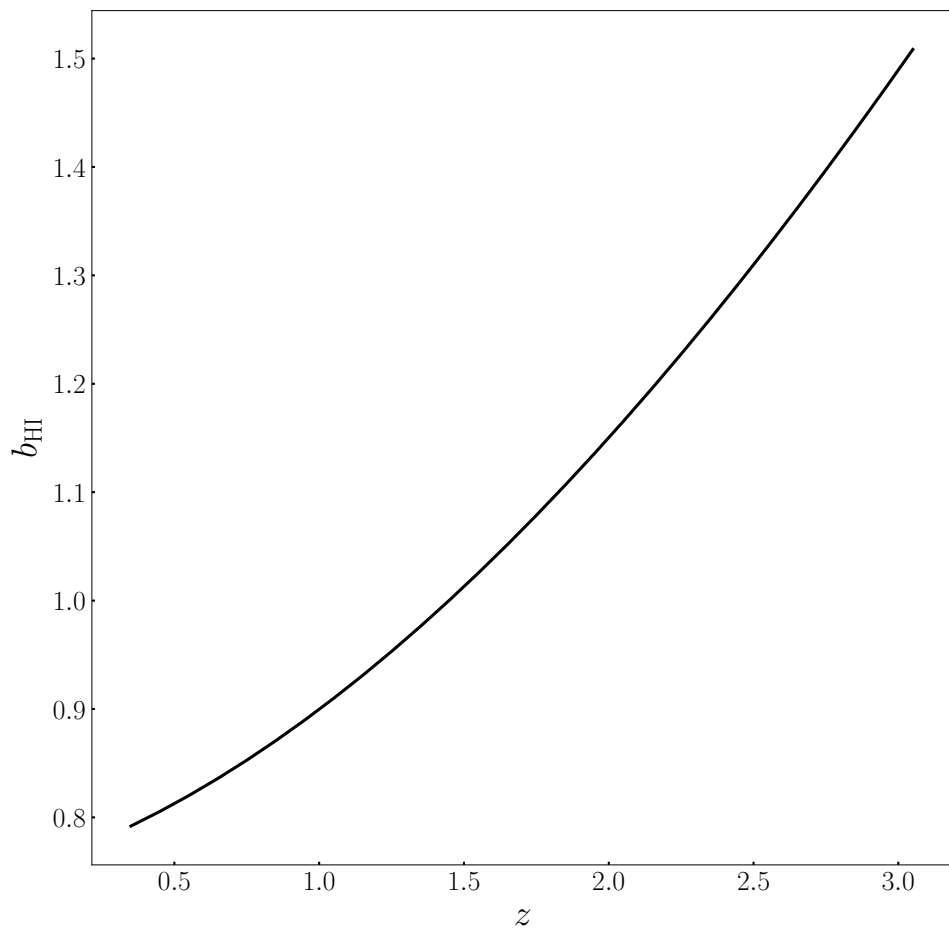


FIGURE 2.7: The HI intensity bias against z .

Chapter 3

Redshift Space Distortions of HI Intensity Mapping

In this brief review of redshift space distortions (RSD), we draw on the references [14, 18–27]

3.1 Linear Redshift Space Distortions

The Hubble redshift is modified by a Doppler correction due to the peculiar velocity of galaxies, which themselves are caused by over- and under-densities in the matter distribution. This induces a distortion of the real-space distribution in redshift space. For example, consider a mild (linear) spherical over-density in real space and consider galaxies at a fixed distance from the centre which have a peculiar velocity $|\mathbf{v}|$ directed towards the centre. For a sufficiently distant observer, these galaxies are all moving away from the observer. They will all share the same Hubble redshift \bar{z} , but the observer will see differences in the observed redshift z . This arises because there is a small correction δz to the observed redshift

$$z = \bar{z} + \delta z, \quad (3.1)$$

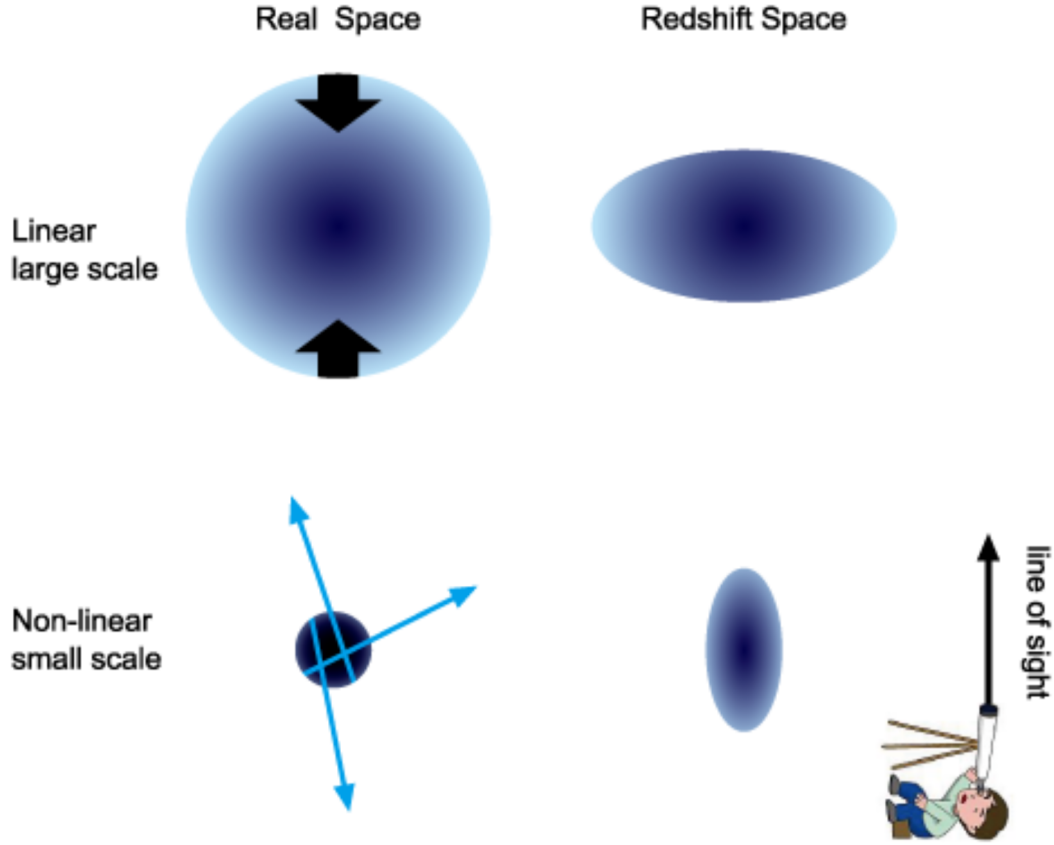


FIGURE 3.1: The diagram above is the relation between real and redshift space on linear to non linear scales [20].

which is due to a Doppler effect:

$$\delta z = (1 + \bar{z})\mathbf{v} \cdot \mathbf{n}, \quad (3.2)$$

where \mathbf{n} is the unit direction from the observer to the galaxy (which is effectively the same for all the galaxies).

Galaxies with velocity orthogonal to the observer line of sight will have $\mathbf{v} \cdot \mathbf{n} = 0$ and therefore $z = \bar{z}$. Galaxies with velocity parallel to the observer line of sight will have the maximum deviation from the Hubble redshift, i.e., $\mathbf{v} \cdot \mathbf{n} = \pm|\mathbf{v}|$. This means that the sphere in real space is distorted into an ellipse that is squashed in the line of sight direction. This is the linear Kaiser RSD effect [28, 29].

Note that the major diameter of the squashed ellipse is the same as the sphere's diameter – which means that the volume of the ellipse is less than the volume of

the sphere. Since the number of galaxies in the sphere is conserved, the number density in redshift space is higher than in real space. In other words, linear RSD lead to an increase in the power spectrum. By conservation of the number of galaxies,

$$n_{g,\text{obs}} d^3 \mathbf{x}_{\text{obs}} = n_g d^3 \mathbf{x}. \quad (3.3)$$

The real and observed comoving positions are:

$$\mathbf{x} = \chi(\bar{z}) \mathbf{n} \quad \text{and} \quad \mathbf{x}_{\text{obs}} = \chi(\bar{z} + \delta z) \mathbf{n}, \quad (3.4)$$

the derivation of the observed comoving position as:

$$\frac{\partial \chi_{\text{obs}}}{\partial \chi} = 1 + \frac{1}{(1 + \bar{z}) \mathcal{H}} \frac{\partial \delta z}{\partial \chi} + \frac{\delta z}{(1 + \bar{z})} \frac{\partial \mathcal{H}}{\partial \chi}, \quad (3.5)$$

we had to neglect the last term on the equation since the Hubble rate changes very little. Using cylindrical coordinates at z -axis along \mathbf{n} :

$$d^3 \mathbf{x}_{\text{obs}} = \frac{\partial \chi_{\text{obs}}}{\partial \chi} d^3 \mathbf{x}. \quad (3.6)$$

Equations (3.2) and (3.5) - (3.6) on (3.3) lead to

$$(1 + \delta_{g,\text{obs}}) \left(1 + \frac{1}{\mathcal{H}(z)} \frac{\partial}{\partial \chi} \mathbf{v} \cdot \mathbf{n} \right) d\chi = (1 + \delta_g) d\chi. \quad (3.7)$$

which then gives at linear order the real-to-redshift space RSD relation between the number overdensities:

$$\delta_{g,\text{obs}} = \delta_g - \frac{1}{\mathcal{H}} \partial_\chi (\mathbf{v} \cdot \mathbf{n}). \quad (3.8)$$

Take a note from the equation (3.3) that the number of galaxies:

$$n_{g,\text{obs}} = \bar{n}_g (1 + \delta_{g,\text{obs}}). \quad (3.9)$$

In Fourier space

$$\partial_\chi(\mathbf{v} \cdot \mathbf{n}) \rightarrow -(\hat{\mathbf{k}} \cdot \mathbf{n})^2 k^2 V_m = -\mu k^2 V_m \quad \text{where} \quad \mu = \hat{\mathbf{k}} \cdot \mathbf{n} = \frac{k_{\parallel}}{k}, \quad (3.10)$$

where we assumed that the galaxy and matter peculiar velocities are equal on linear scales:

$$V = V_m. \quad (3.11)$$

By the perturbed conservation equation

$$\delta'_m = k^2 V_m. \quad (3.12)$$

The definition of the growth factor and growth rate gives

$$\delta'_m = f\mathcal{H}\delta_m. \quad (3.13)$$

Putting it all together (3.8) becomes

$$\delta_{g,\text{obs}}(\eta, k, \mu) = [b(\eta) + f(\eta)\mu^2]\delta_m(\eta, k). \quad (3.14)$$

Then the linear observed galaxy power spectrum is

$$P_{g,\text{obs}} = [b + f\mu^2]^2 P_m. \quad (3.15)$$

For HI intensity mapping, all the previous arguments still apply:

$$P_{\text{HI,obs}} = [b_{\text{HI}} + f\mu^2]^2 P_m. \quad (3.16)$$

From now on we will drop the ‘obs’ from $P_{\text{HI,obs}}$.

3.2 Nonlinear Redshift Space Distortions

On large scales, galaxies with small infall peculiar velocities lead to a squashing along the line of sight. Considering non-linear scales, the peculiar velocities are large around a strong overdensity and this causes a stretching along the line of sight, as shown in Figure 3.1. This is known as the ‘Fingers of God’ (FoG) effect. It is often modelled by one of three damping factors, known as Lorentzian, Gaussian and Lorentzian-squared respectively:

$$D_{\text{FoG}}(z, k, \mu) = \begin{cases} [1 + \frac{1}{2}\mu^2 k^2 \sigma^2(z)]^{-1}, \\ \exp[-\frac{1}{2}\mu^2 k^2 \sigma^2(z)], \\ [1 + \frac{1}{2}\mu^2 k^2 \sigma^2(z)]^{-2}, \end{cases} \quad (3.17)$$

where σ is damping parameter of the galaxies. In practice, $\sigma(z)$ can also be modelled from simulations. We use the model from simulations given in [23]:

$$\sigma(z) = \sigma(0)(1+z)^{-m} \exp\left[-\left(\frac{z}{z_p}\right)^2\right], \quad (3.18)$$

$$\sigma(0) = 11.0, \quad m = 1.9 \quad \text{and} \quad z_p = 11.0. \quad (3.19)$$

This relation (3.18) is on Figure 3.2, the damping parameter against redshift z . It shows that the model is more strongly damped at the lower redshifts. There is a reduction of power on non-linear scales due to this FoG effect:

$$P_{\text{HI}}^{NL}(z, k, \mu) = D_{\text{FoG}}(z, k, \mu)[b_{\text{HI}}(z) + f(z)\mu^2]^2 P_m^{NL}(z, k). \quad (3.20)$$

P_m^{NL} is the matter power spectrum including non-linear scales. It is computed in CLASS with the HALOFIT option. The bias for HI intensity mapping is given by (2.81). Note that we keep the linear bias and include nonlinear matter clustering via P_m^{NL} .

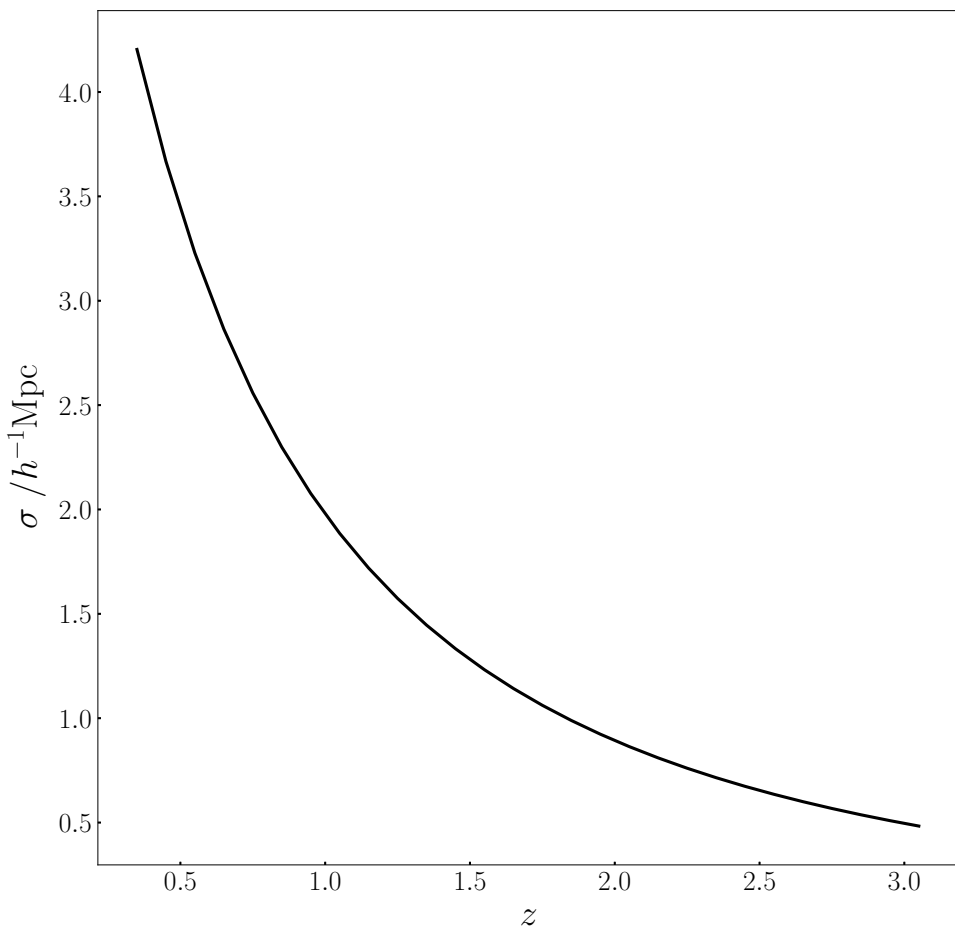


FIGURE 3.2: The HI damping parameter against z .

3.3 Multipole expansion of power spectrum

The dependance on μ of the power spectrum can be expanded out in Legendre polynomials. Usually the first three even multipoles, monopole $\ell = 0$, quadrupole $\ell = 2$ and hexadecapole $\ell = 4$:

$$P_{\text{HI}}^\ell(z, k) = \frac{2\ell + 1}{2} \int_{-1}^1 d\mu P_{\text{HI}}(z, k, \mu) \mathcal{L}_\ell(\mu) \quad (3.21)$$

For the linear power spectrum (without FoG damping) we get the following multipoles:

$$\begin{aligned} P_{\text{HI}}^0(z, k) &= \left(b^2 + \frac{2}{3}bf + \frac{1}{5}f^2\right) P_m(z, k), \\ P_{\text{HI}}^2(z, k) &= \left(\frac{4}{3}bf + \frac{4}{7}f^2\right) P_m(z, k) \\ P_{\text{HI}}^4(z, k) &= \left(\frac{8}{35}f^2\right) P_m(z, k). \end{aligned} \quad (3.22)$$

The ratios $P_{\text{HI}}^2(z, k)/P_{\text{HI}}^0(z, k)$ and $P_{\text{HI}}^4(z, k)/P_{\text{HI}}^0(z, k)$ on linear scales is independent of the wave vector k at any redshift. This is clear from Figure 3.3. We used (3.22) above at different redshifts $z = 0.0, 0.5, 1.0, 1.5$. The difference between monopole and quadrupole decreases with redshift – this reflects the fact that RSD anisotropy grows as structure growth develops. Take note that multipoles are always above the power of the real space power due to contribution of Kaiser term.

Figure 3.4 shows the effect of nonlinearity on the monopole of the HI power spectrum in real and redshift space. The plots in this figure are based on simulations [22], and they show where the linear Kaiser model breaks down, for $0 \leq z \leq 5$. It is clear that at high redshift the linear model works well, but it breaks down on larger scales as the redshift reduces.

We can illustrate the effect on nonlinearity using the FoG model (3.20). We

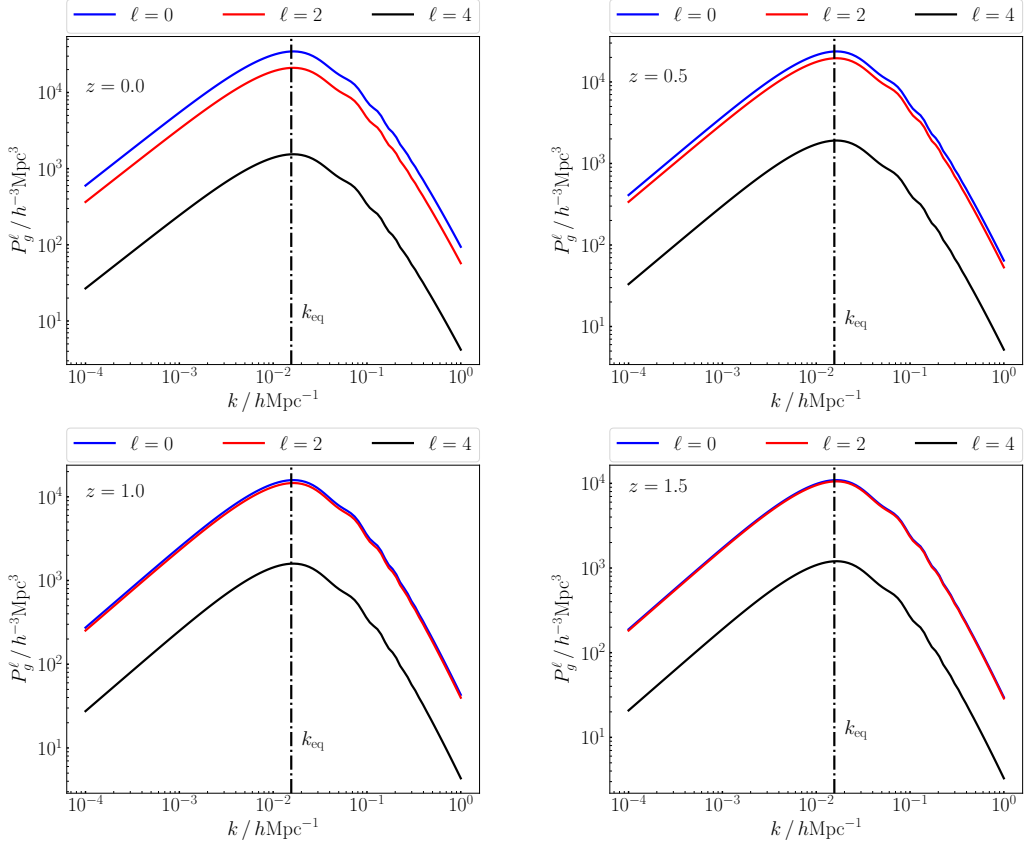


FIGURE 3.3: Multipoles of the observed linear galaxy power spectrum at $z = 0.0, 0.5, 1.0, 1.5$, left to right, top to bottom. Blue, red and black lines represent the monopole, quadrupole and hexadecapole respectively. Dash-dotted black line is the equality scale.

apply the same Legendre expansion (3.21) to get multipoles that include non-linear scales:

$$P_{\text{HI}}^\ell(z, k) = \frac{2\ell+1}{2} \int_{-1}^1 d\mu P_{\text{HI}}^{NL}(z, k, \mu) \mathcal{L}_\ell(\mu). \quad (3.23)$$

We will use the Lorentzian damping factor, so that

$$P_{\text{HI}}^{NL}(z, k, \mu) = [b_{\text{HI}} + f\mu^2]^2 \left(1 + \frac{1}{2}\kappa^2\mu^2\right)^{-1} P_m^{NL}(k). \quad (3.24)$$

We have defined the dimensionless quantity

$$\kappa(z) = \frac{k}{k_D(z)} \quad \text{where} \quad k_D(z) = \frac{\sqrt{2}}{\sigma(z)}. \quad (3.25)$$

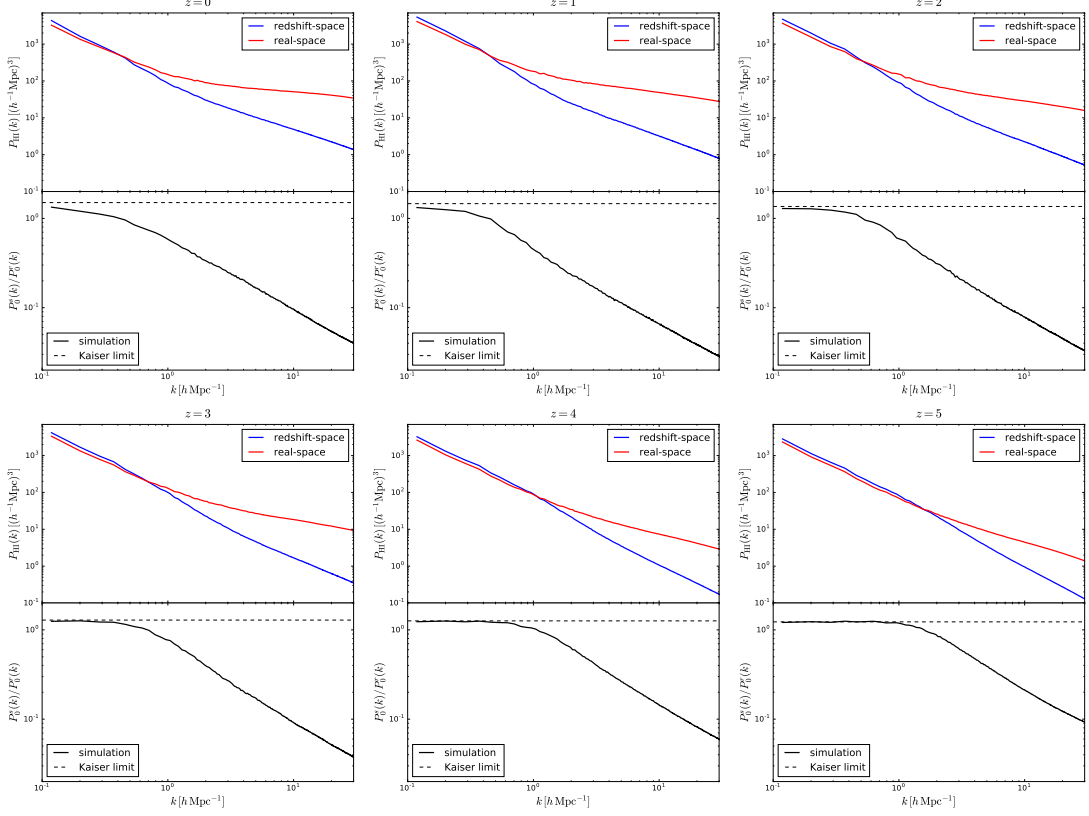


FIGURE 3.4: Impact of RSD on the HI power spectrum at redshifts 0 (top-left), 1 (top-middle), 2 (top-right), 3 (bottom-left), 4 (bottom-middle) and 5 (bottom-right). Simulations are compared to the linear model. The upper part of each panel shows the HI power spectrum (monopole) in real space (red) and redshift space (blue). The bottom part displays the ratio between the monopoles in redshift and real space (solid black) and the prediction of linear theory (dashed black). RSD enhance/ suppress power on large/ small scales. Linear theory can explain the HI clustering in redshift space down to very small scales at high-redshift, while it cannot at low redshift on the scales we probe in the simulations.

(From [22].)

k_D is the damping scale, so that $\kappa > 1$ is the strong damping regime and $\kappa < 1$ is the weak damping regime. σ is given by (3.18).

Then (3.23) gives the following multipoles:

$$\frac{P_{\text{HI}}^{NL,0}}{P_m^{NL}} = \frac{\tan^{-1}(\kappa)}{\kappa} \left(b^2 - \frac{2bf}{\kappa^2} + \frac{f^2}{\kappa^4} \right) + \frac{2bf}{\kappa^2} + f^2 \left(\frac{1}{3\kappa^2} - \frac{1}{\kappa^4} \right) \quad (3.26)$$

$$\begin{aligned} \frac{P_{\text{HI}}^{NL,2}}{P_m^{NL}} &= -\frac{\tan^{-1}(\kappa)}{\kappa} \left(b^2 \left(\frac{5}{2} + \frac{15}{2k^2} \right) - \frac{5bf}{\kappa^2} + f^2 \left(\frac{15}{2\kappa^6} + \frac{5}{\kappa^4} \right) \right) + \frac{15b^2}{\kappa^2} - \frac{15bf}{\kappa^4} \\ &\quad + f^2 \left(\frac{2}{3\kappa^2} + \frac{15}{2\kappa^6} \right) \end{aligned} \quad (3.27)$$

$$\begin{aligned} \frac{P_{\text{HI}}^{NL,4}}{P_m^{NL}} &= \frac{9\tan^{-1}(\kappa)}{8} \left(b^2 \left(\frac{3}{\kappa} + \frac{30}{\kappa^3} + \frac{35}{\kappa^5} \right) - bf \left(\frac{6}{\kappa^3} + \frac{60}{\kappa^5} + \frac{70}{\kappa^7} \right) + f^2 \left(\frac{3}{\kappa^5} + \frac{30}{k^7} + \frac{35}{\kappa^9} \right) \right) \\ &\quad + b^2 \left(\frac{105}{8\kappa^2} \right) - bf \left(\frac{27}{4\kappa^2} + \frac{105}{4\kappa^4} \right) + f^2 \left(\frac{45}{16\kappa^4} + \frac{105}{8\kappa^6} \right). \end{aligned} \quad (3.28)$$

For $\kappa \ll 1$, all multipoles approach the undamped form, but for $\kappa \gg 1$ the multipoles become strongly damped and the quadrupole and hexadecapole can become negative. (The monopole is always positive.) As we go to smaller scales the effect of FoG gets stronger on anisotropy. This is shown in Figure 3.5.

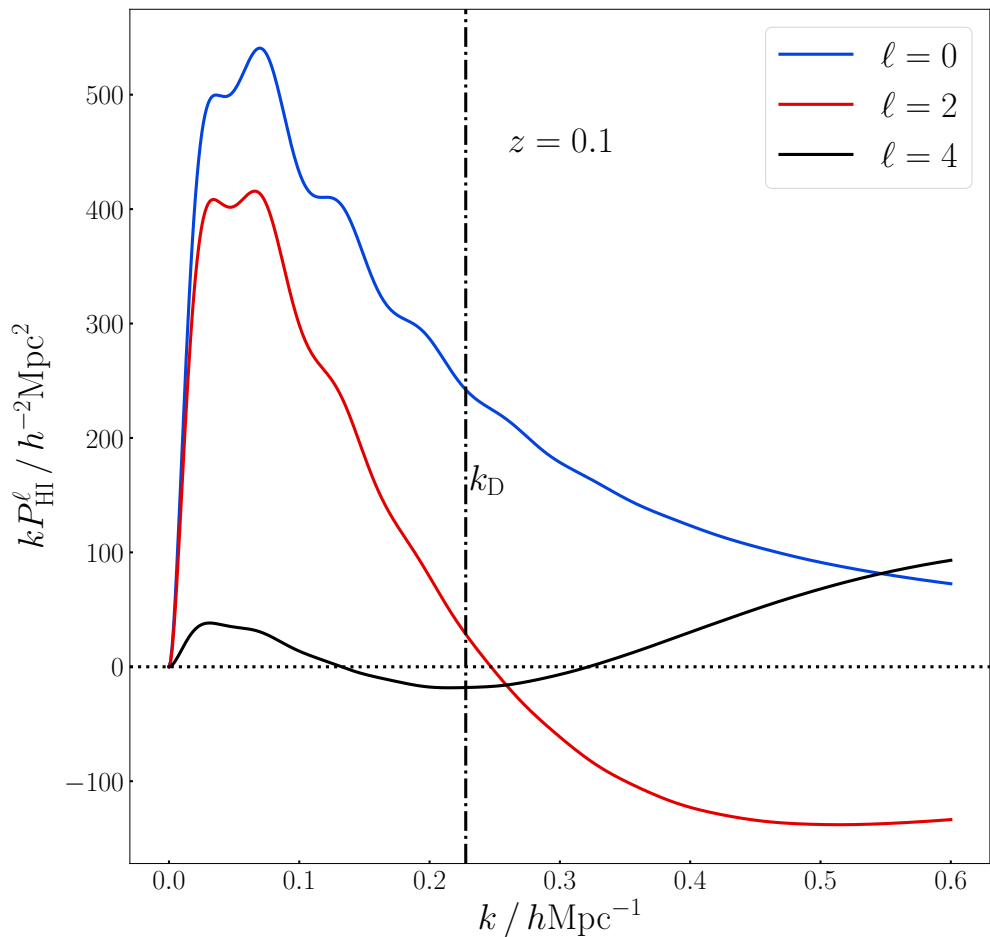


FIGURE 3.5: Multipoles of the HI power spectrum at $z = 0.1$ with Gaussian FoG damping, using (3.18), which determines k_D (black dash-dot line).

3.4 HI power spectrum in k-space

Using

$$\mu = \mathbf{n} \cdot \hat{\mathbf{k}} = \frac{k_{\parallel}}{k} = \frac{k_{\parallel}}{\sqrt{k_{\perp}^2 + k_{\parallel}^2}}, \quad (3.29)$$

$$k_{\perp} = k \sqrt{1 - \mu^2}, \quad (3.30)$$

we can rewrite the linear power spectrum as

$$P_{\text{HI}}(k_{\parallel}, k_{\perp}) = \left[b + f \frac{k_{\parallel}^2}{k_{\perp}^2 + k_{\parallel}^2} \right]^2 P_m(k), \quad (3.31)$$

where we dropped the z -dependence for convenience. We can use this to make a colour plot of P_{HI} in the $(k_{\perp}, k_{\parallel})$ -plane; see Figure 3.6. Figure 3.6 shows the

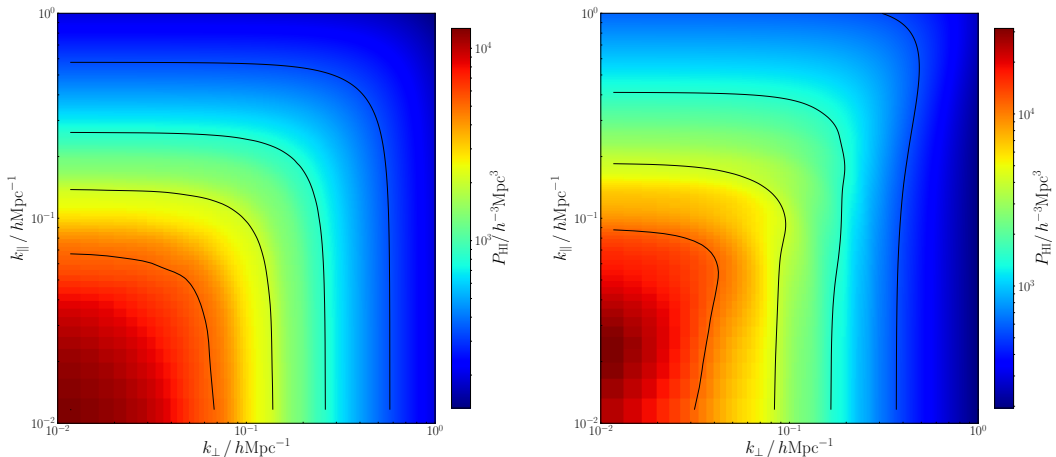


FIGURE 3.6: Colour map of linear HI power spectrum in real space (*left*) and redshift space (*right*) at $z = 0.1$. Black lines are iso-power contours.

HI power spectrum contours in real space are isotropic (here we have distorted contours due to log scales), whereas in redshift space the anisotropy is apparent.

Figure 3.6 shows the colour plot for Gaussian and Lorentzian damping factors. We can see that along the line of sight k_{\parallel} , the contours of constant P_{HI} are closer together because P_{HI} is decreasing more steeply. When we compare between the

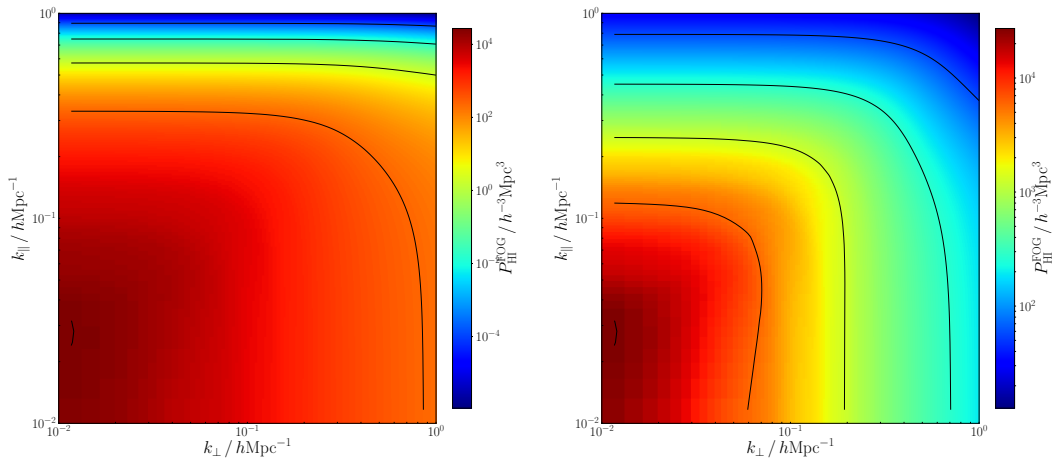


FIGURE 3.7: Colour map of HI power spectrum with a Gaussian (*left*) and Lorentzian (*right*) damping factor, at $z = 0.1$

two plots in Figure 3.7, it is clear that the Gaussian damping factor is stronger than the Lorentzian one.

Chapter 4

Measuring the Redshift-space Power Spectrum with MeerKAT and SKA

HI intensity mapping allows us to probe the universe structure and expansion. We want to measure large volumes to achieve statistical precision. If we do observations with galaxy surveys we spend quite a lot of time to detect each galaxy and measure its redshift. By contrast, intensity mapping does not resolve galaxies but still can map large areas of the sky rapidly (in single-dish mode). The disadvantage is that intensity mapping has strong foreground contamination, but there are advanced techniques to deal with that and they are being improved constantly. We can map large sky areas with very high redshift accuracy.

In this Chapter we investigate how well MeerKAT and SKA can measure the power spectrum of HI intensity. We take account of foreground contamination, instrumental effects and thermal noise.

4.1 Modelling the Power Spectrum

Intensity mapping has excellent radial resolution (i.e., redshift accuracy) but poor angular resolution in single-dish mode. This is modelled by a damping of small-scale angular modes, i.e. large k_{\perp} , through the telescope beam [30]:

$$D^{\text{beam}}(z, k, \mu) = \exp \left[-\frac{(1 - \mu^2)k^2 r(z)^2 \theta_b(z)^2}{8 \ln 2} \right]. \quad (4.1)$$

The beam only affects HI power along the perpendicular modes k_{\perp} . In (4.1),

$$\theta_b(z) = 1.22 \frac{\lambda_{21}(1+z)}{D_d}, \quad (4.2)$$

where the comoving distance is $r(z)$ and the diameter of the telescope is D_d . The effect of the beam is then given by

$$P_{\text{HI}}(z, k, \mu) \rightarrow D^{\text{beam}}(z, k, \mu) P_{\text{HI}}(z, k, \mu). \quad (4.3)$$

In addition to the beam, we have to take account of the effects of foreground cleaning. Removal of foreground contamination for single-dish intensity mapping results in a loss of large-scale radial modes [30]. We model this by a cut-off [31]:

$$|k_{\parallel}| > k_{\text{fg}} \approx 0.01 h \text{ Mpc}^{-1}. \quad (4.4)$$

Combining the beam and foreground effects, the power spectrum (3.20) becomes

$$P_{\text{HI}}(z, k, \mu) = \Theta(|k_{\parallel}| - k_{\text{fg}}) D^{\text{beam}}(z, k, \mu) D_{\text{FoG}}(z, k, \mu) [b_{\text{HI}}(z) + f(z)\mu^2]^2 P_m^{NL}(z, k), \quad (4.5)$$

where Θ is the Heaviside step function.

This is the model that we are using to measure the growth rate parameter through the proposed MeerKAT Large Area Synoptic Survey (MeerKLASS) and the Square

Kilometre Array Phase 1 (SKA1). In Table 4.1 we show the instrumental parameters of these two experiments that we are going to use.

Survey	Redshift (z)	Dishes (N_d)	Dish size (D_d)	Total time (hr)	S_{area} deg^2
MeerKAT-Low band	0.1 – 0.58	64	13.5m	4000	4000
MeerKAT-UHF band	0.45 – 1.45	64	13.5m	4000	4000
SKA1 band 1	0.35 – 3.0	197	15m	10000	20000
SKA1 band 2	0.1 – 0.49	197	15m	10000	20000

TABLE 4.1: The specifications of MeerKAT and SKA [32].

Demonstrating the effects of beam and foreground cleaning for this SKA Band 1, we show the multipoles expansion ($\ell = 0, 2, 4$) of (4.5) in Figure 4.1. The results in Figure 4.1 are computed at redshift $z = 0.5$. We use the Gaussian damping factor (3.17).

If we include the foreground cut in the model we expect to see damping at small k and we indicate the result in solid lines. But when we look at the figure, we realise that there are some interesting features in these different multipoles. The monopole (blue solid line) P_{HI}^0 shows the expected damping when adding the foreground cut. But for the quadrupole (red solid line) the power is boosted by the foreground cleaning. The reason is that during the foreground cleaning the negative contribution in the quadrupole is removed, while the monopole multipole contains only positive contributions. (Compare the similar results in [24].)

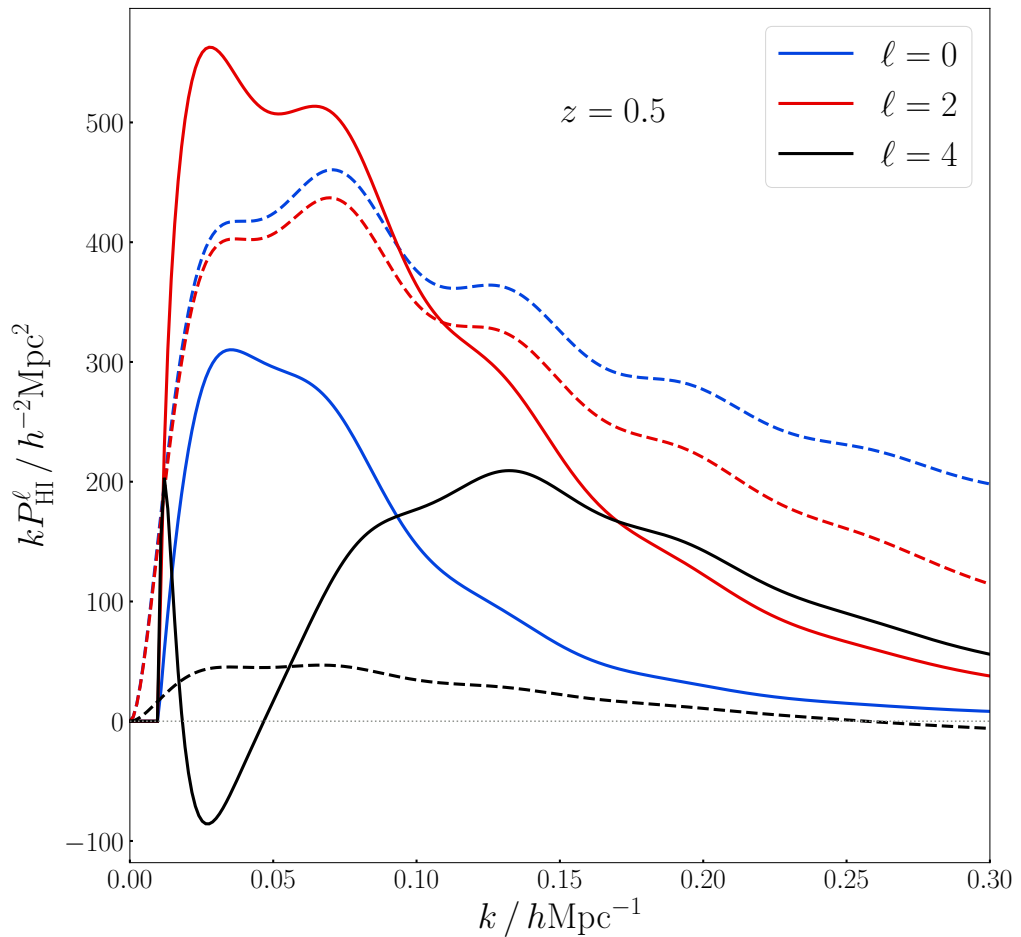


FIGURE 4.1: Power spectrum multipoles of HI intensity mapping using SKA Band 1 at redshift $z = 0.5$. The multipoles without the beam and foreground cut effect, represented in dashed lines and multipoles with both effects (beam and foreground cut) represented in solid lines.

4.2 Signal to Noise of the Power Spectrum

We have included telescope beam and foreground removal effects in our model of the redshift space power spectrum in the previous section. In order to measure the detectability of this power spectrum, we need to include the effects that reduce the signal in the power spectrum:

- *Thermal noise*: The temperature of the sky (i.e. mainly the Galactic emissions) and of the dishes contribute to the instrumental noise of the telescope, together with some of the survey properties (see below). Note that for the scales that we consider, thermal noise is much greater than shot noise [22] and we neglect the shot noise.
- *Cosmic variance*: The power spectrum is a measure of correlations between temperature contrast at different scales. For long-wavelength modes, there are less possible measurements than for short-wavelength modes. This effect, called cosmic variance [2], means that the signal is weaker on large scales than on small scales.

These two effects combine to form the variance of the power spectrum [33]:

$$\text{var}[P_{\text{HI}}(z, k, \mu)] = \frac{k_f^3(z)}{\pi k^2 \Delta k \Delta \mu} [\tilde{P}_{\text{HI}}(z, k, \mu)]^2, \quad (4.6)$$

The step sizes $\Delta\mu$ and Δk are chosen according to numerical considerations. The fundamental mode k_f is defined by the comoving volume of a redshift bin centred at redshift z (see Figure 4.2):

$$k_f(z) = \frac{2\pi}{V(z)^{1/3}}, \quad (4.7)$$

where

$$V(z) = \frac{4\pi f_{\text{sky}}}{3} \left[r(z + \Delta z/2)^3 - r(z - \Delta z/2)^3 \right], \quad (4.8)$$

and the sky fraction covered by the survey is

$$f_{\text{sky}} = \frac{S_{\text{area}}}{S_{\text{total}}}, \quad \text{where} \quad S_{\text{total}} = 4\pi \left(\frac{180}{\pi}\right)^2 \text{deg}^2. \quad (4.9)$$

The volume against redshift is shown in Figure 4.2.

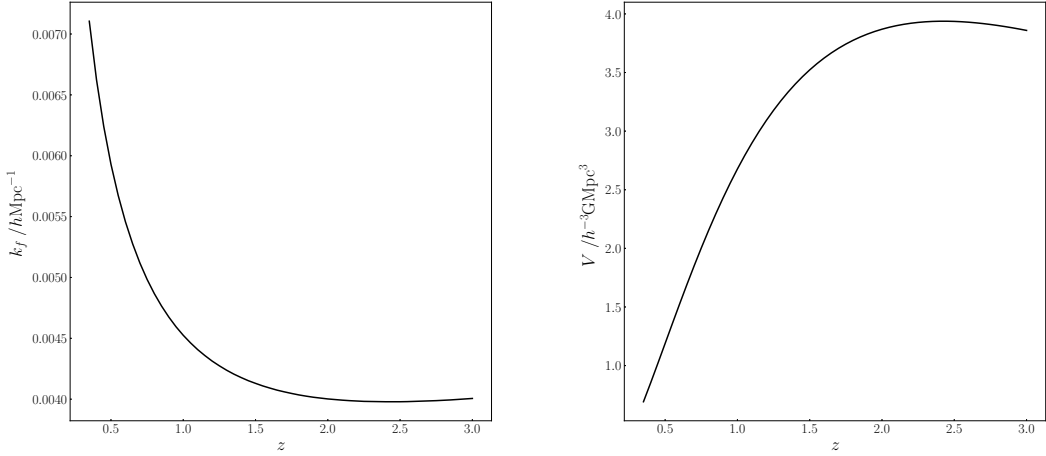


FIGURE 4.2: The fundamental mode function (*left*) and volume function (*right*) against bin redshift.

In (4.6) the

$$\tilde{P}_{\text{HI}}(z, k, \mu) = P_{\text{HI}}(z, k, \mu) + P_{\text{noise}}, \quad (4.10)$$

and the noise power spectrum is [30, 31]

$$P_{\text{noise}} = 2\pi f_{\text{sky}} \frac{r^2(1+z)^2}{N_{\text{d}} H(z) \nu_{21} t_{\text{tot}}} \left(\frac{T_{\text{sys}}}{T_{\text{HI}}}\right)^2. \quad (4.11)$$

The t_{tot} is the total survey time and N_{d} is the number of dishes (see Table 4.1). T_{sys} is the system temperature, made up of the sky plus receiver temperatures (see Tables 4.2 and 4.3). The noise power spectra for MeerKAT and SKA are shown in Fig. 4.3. Since we divide the thermal noise power by the square of the background temperature T_{HI} , it has the same units, $h^{-3}\text{Mpc}^3$, as the HI power spectrum.

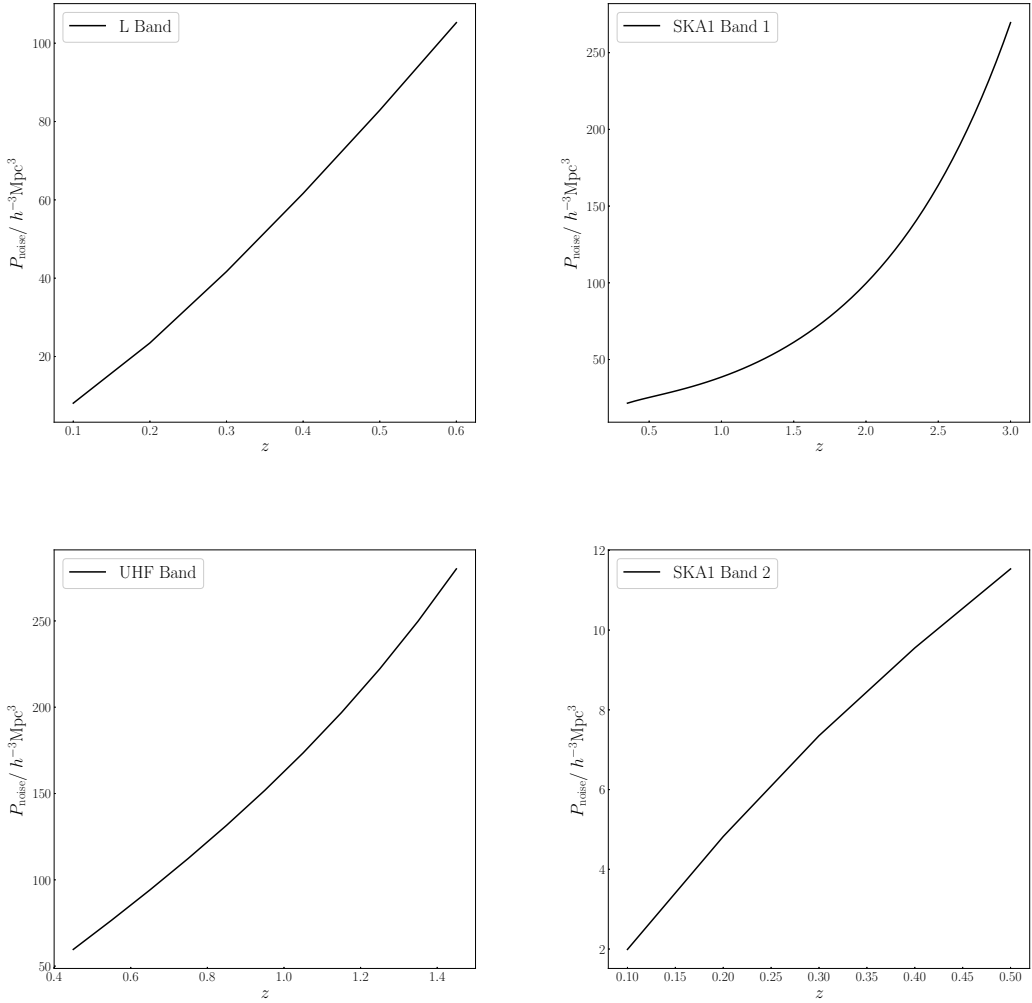


FIGURE 4.3: The noise power spectra for MeerKAT in L-Band and UHF-Band (left) and SKA in Bands 1 and 2 (right).

The signal squared divided by the variance gives the signal-to-noise ratio (SNR) squared. In the Gaussian case of independent k -bins, the SNR in the redshift bin centred on z is given by the following sum over wavenumber and orientation [33, 34]:

$$\left[\frac{S}{N}(z) \right]^2 = \sum_{\mu=-1}^{+1} \sum_{k_{\min}(z)}^{k_{\max}(z)} \frac{1}{\text{var}[P_{\text{HI}}(z, k, \mu)]} [P_{\text{HI}}(z, k, \mu)]^2, \quad (4.12)$$

where

$$P_{\text{HI}} = \Theta(|k_{\parallel}| - k_{\text{fg}}) D^{\text{beam}} D_{\text{FoG}} (b_{\text{HI}} + f\mu^2)^2 P_m^{NL}. \quad (4.13)$$

The wavenumber sum is over the range

$$k_{\min}(z) = k_f(z), \quad (4.14)$$

$$k_{\max}(z) = 0.2 h(1+z)^{2/(2+n_s)}. \quad (4.15)$$

The minimum k is estimated by the fundamental mode k_f . The maximum k is chosen to exclude scales where dark matter clustering is becoming nonlinear [31].

The step sizes in wavenumber and μ are chosen as [31]

$$\Delta k(z) = k_f(z), \quad \Delta \mu = 0.04. \quad (4.16)$$

4.3 Signal to Noise for MeerKAT

We use the information in Section 4.2, together with Table 4.2, to compute the SNR of the HI intensity power spectrum that is expected from the MeerKAT survey: sky area 4000 deg^2 ($f_{\text{sky}} = 0.097$), with observing time 4000 hr, over redshifts $0.05 \leq z \leq 0.58$ in the L Band and $0.4 \leq z \leq 1.45$ in the UHF Band (see Table 4.1). The system temperature for MeerKAT is given in Table 4.2 and the interpolated curve is shown in Figure 4.4.

z	L–Band $T_{\text{sys}}(K)$	z	UHF–Band $T_{\text{sys}}(K)$
0.014	17.95	0.420	20.32
0.052	18.33	0.495	20.95
0.092	18.75	0.578	21.67
0.136	19.21	0.671	22.50
0.183	19.72	0.775	23.48
0.235	20.27	0.893	24.66
0.291	20.88	1.029	26.11
0.352	21.55	1.185	27.94
0.420	22.29	1.367	30.30
0.495	23.11	1.448	31.45
0.578	24.04		

TABLE 4.2: The system temperature for MeerKAT for L and UHF Bands (from [32]).

Using (4.12), we compute the SNR for each redshift bin, using a bin-width of

$$\Delta z = 0.1. \quad (4.17)$$

For the FoG damping factor, we use the Gaussian model. The results are shown in the left panels of Figure 4.5, for L Band (top) and UHF band (bottom).

The cumulative SNR is defined by adding the per-bin SNR in quadrature:

$$\left[\frac{S}{N}(\leq z_n) \right]^2 = \sum_{i=1}^n \left[\frac{S}{N}(z_i) \right]^2, \quad (4.18)$$

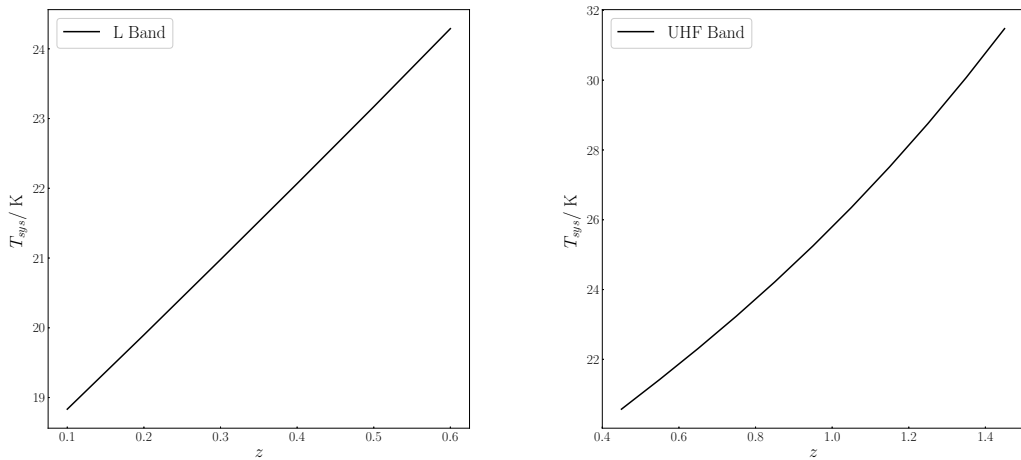


FIGURE 4.4: System temperature for MeerKAT.

This is shown in the right panels of Figure 4.5. The plots are also given for the cases without telescope beam effects and without foreground cleaning cut (blue curves); with beam effects included (red) and with beam effects plus foreground effects included (black).

It is clear that the SNR is strongly suppressed by beam and foreground effects – especially for the higher-redshift UHF Band. The beam effect makes the largest contribution to the suppression of SNR. But when we look at L-Band the top panels on Figure 4.5, the beam and foreground cleaning suppress SNR strongly at $z_{bin} \approx > 0.20$. This is because of the foreground contaminations removed that dominates at high redshift. It is clear that the HI intensity mapping is a poor resolution experiment and is the reason why there is a loss of signal at high redshift. Hence we still have enough power even when we include all the effects on HI power spectrum that can lead us on measuring the growth rate factor on both MeerKAT Bands.

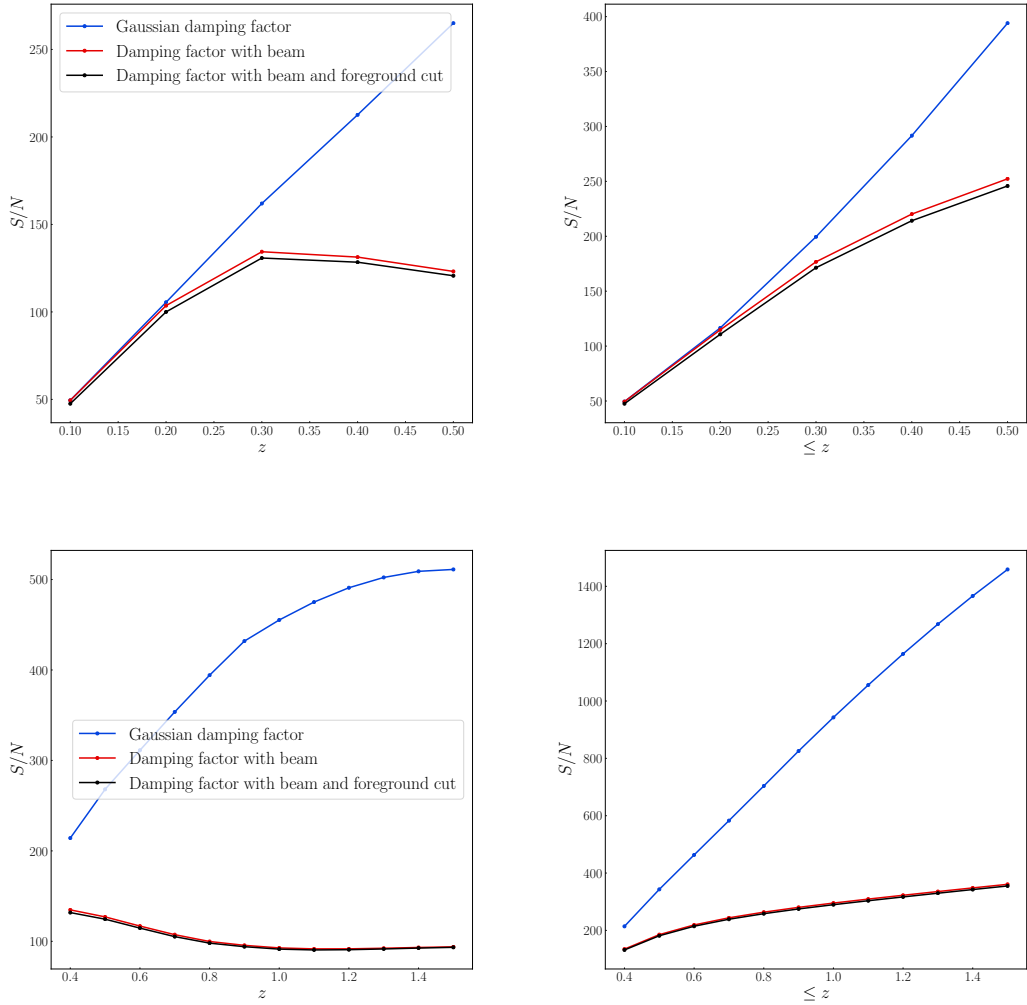


FIGURE 4.5: The SNR of the HI intensity power spectrum for the MeerKAT surveys in L Band (top panels) and UHF Band (bottom panels). The left panels show SNR per redshift bin; the right panels show the cumulative SNR at each redshift bin. Blue lines include only the FoG effects, without beam or foreground effects. With beam effects included, we have the red lines and with foreground effects added to beam effects, we get the black lines.

4.4 Signal to Noise for SKA

We repeat the previous computations for the SKA surveys: sky area of 20000deg^2 , which gives $f_{sky} = 0.048$, with total time 10000hr, in Band 2 ($0.10 \leq z \leq 0.49$) and Band 1 ($0.3 \leq z \leq 3.0$). Experimental parameters are given in Table 4.1. The system temperature for SKA1 is shown in Table 4.3 (from [32]) and plotted in Figure 4.6.

z	Band 1 $T_{\text{sys}}(K)$	z	Band 2 $T_{\text{sys}}(K)$
0.341	27.73	0.017	16.10
0.403	27.23	0.064	16.24
0.470	26.91	0.115	16.40
0.539	26.80	0.168	16.59
0.618	26.87	0.223	16.80
0.688	27.11	0.280	17.04
0.767	27.52	0.341	17.31
0.850	28.10	0.403	17.61
0.938	28.84	0.470	17.96
1.029	29.75		
1.125	30.83		
1.225	32.09		
1.330	33.55		
1.439	35.20		
1.554	37.08		
1.675	39.19		
1.801	41.57		
1.933	44.24		
2.071	47.24		
2.216	50.61		
2.367	54.39		
2.526	58.64		
2.692	63.40		
2.866	68.75		
3.048	74.77		

TABLE 4.3: The system temperature for SKA in Bands 1 and 2 [32].

The results are shown in the left panels of Figure 4.7, for Band 1 (top) and Band 2 (bottom). The cumulative SNR is shown in the right panels. The plots are

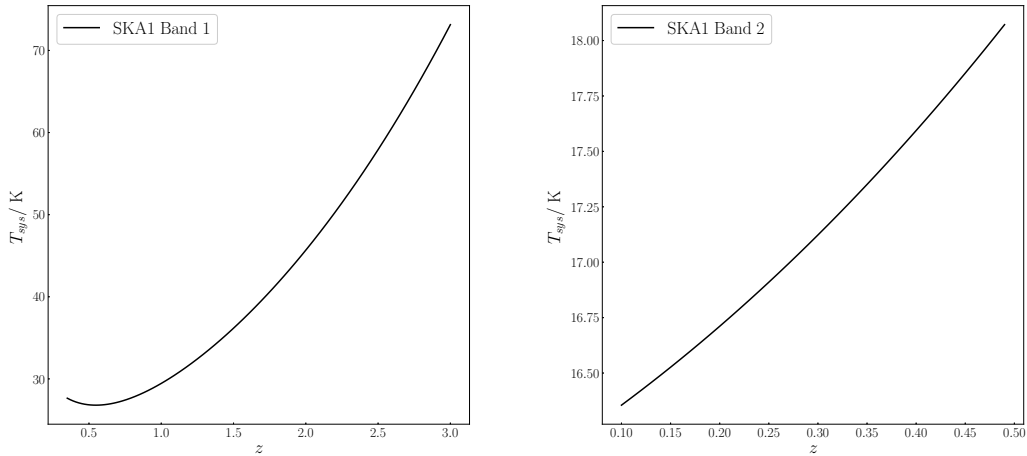


FIGURE 4.6: System temperature for SKA in Bands 1 and 2.

also given for the cases without telescope beam effects and without foreground cleaning cut (blue curves); with beam effects included (red) and with beam effects plus foreground effects included (black).

It is clear that the SNR is strongly suppressed by beam and foreground effects – especially for the higher-redshift Band 1. The beam effect makes the largest contribution to the suppression of SNR. When we look at Band 2 the bottom panels on Figure 4.7, the telescope beam and foreground cleaning suppress SNR strongly at $z_{\text{bin}} \approx > 0.20$, meaning that foreground contamination removed occurred muchly at $z_{\text{bin}} \approx > 0.20$.

Finally, we show the comparison between MeerKAT and SKA in Figure 4.8 when all the effects included on the surveys (telescope beam, foreground cleaning). We can see that the SKA Band 1 contains much SNR compared to all the Bands indicated on the Figure.

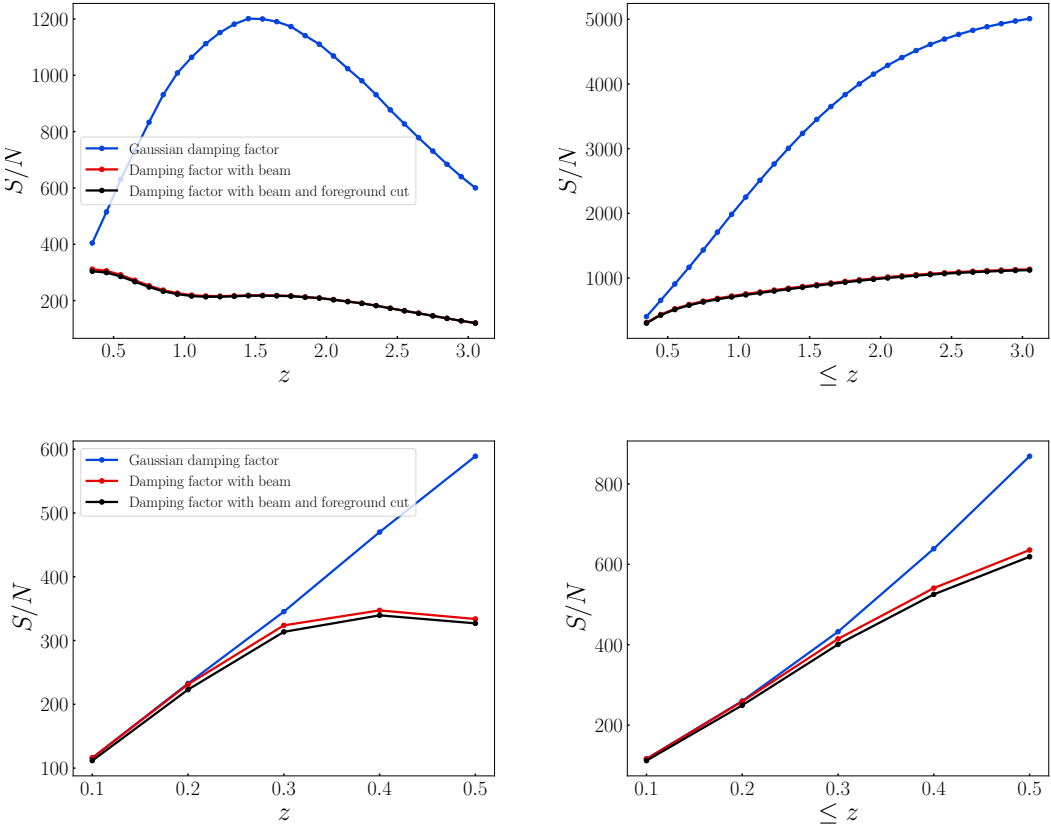


FIGURE 4.7: The SNR of the HI intensity power spectrum for the SKA surveys in Band 1 (top panels) and Band 2 (bottom panels). The left panels show SNR per redshift bin; the right panels show the cumulative SNR at each redshift bin. Blue lines include only the FoG effects, without beam or foreground effects. With beam effects included, we have the red lines and with foreground effects added to beam effects, we get the black lines.

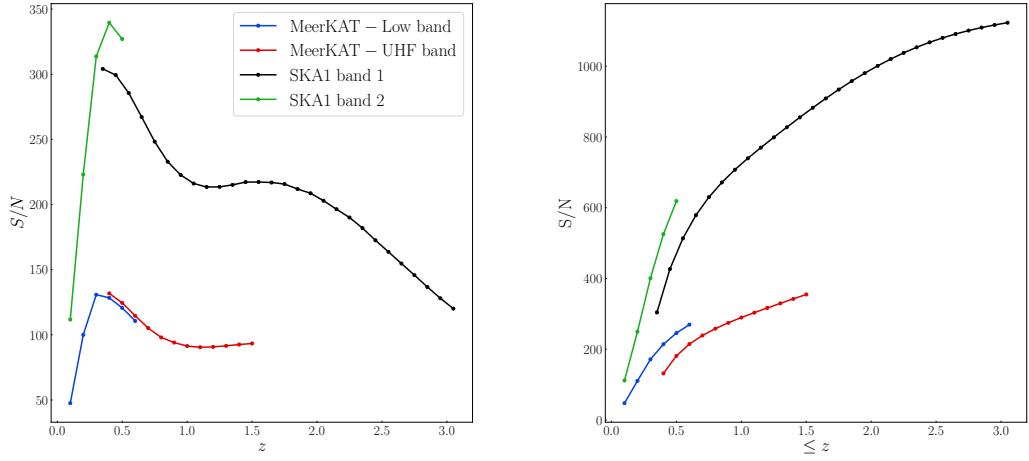


FIGURE 4.8: The SNR of HI intensity mapping with MeerKAT and SKA1 survey (left panel) and cumulative SNR (right panel).

Chapter 5

Fisher Forecasts for MeerKAT and SKA

MeerKAT is operational since 2019 and SKA1 is in the pre-construction phase. They will produce three-dimensional maps of the integrated intensity of the 21cm emission. Before data is available, we can make predictions using the Fisher Forecast formalism to estimate the precision with which MeerKAT and SKA1 can measure the growth rate in large-scale structure. It allows us to forecast for cosmological and astrophysical parameters. Here we focus on two parameters: the growth index, γ , and the normalized amplitude of the power spectrum, $\sigma_{8,0}$. This means that we fix the standard cosmological parameters to their Planck 2018 fiducial values – effectively assuming that these are constrained by Planck and other existing supernova and BAO surveys. We also fix the main astrophysical parameters, i.e. the HI clustering bias $b_{\text{HI}}(z)$ and damping function $\sigma(z)$, to the models given in Chapter 3.

5.1 Fisher Forecast Formalism

The Fisher matrix in a redshift bin centred at z_i , for a set of constant parameters θ_α , is [2, 31, 35, 36]:

$$F_{\alpha\beta}(z_i) = \sum_{\mu=-1}^{+1} \sum_{k_{\min}(z)}^{k_{\max}(z)} \frac{1}{\text{var}[P_{\text{HI}}(z_i, k, \mu)]} \frac{\partial P_{\text{HI}}(z_i, k, \mu)}{\partial \theta_\alpha} \frac{\partial P_{\text{HI}}(z_i, k, \mu)}{\partial \theta_\beta}, \quad (5.1)$$

where the power spectrum is given in (4.5) and the variance is given by (4.6)–(4.11). The cumulative Fisher matrix up to redshift bin n is

$$F_{\alpha\beta}(\leq z_n) = \sum_{i=1}^n F_{\alpha\beta}(z_i). \quad (5.2)$$

The derivatives with respect to the two parameters of interest are:

$$\frac{\partial P_{\text{HI}}}{\partial \gamma} = \frac{\partial f}{\partial \gamma} \frac{\partial P_{\text{HI}}}{\partial f} = \frac{2(\ln \Omega_m) f \mu^2}{[b_{\text{HI}} + f \mu^2]} P_{\text{HI}}, \quad (5.3)$$

$$\frac{\partial P_{\text{HI}}}{\partial \sigma_{8,0}} = \frac{2}{\sigma_{8,0}} P_{\text{HI}}. \quad (5.4)$$

Here we used the fact that the matter power spectrum depends on $\sigma_{8,0}$ as

$$P_m(z, k) = (\sigma_{8,0})^2 \mathcal{P}_m(z, k), \quad (5.5)$$

where \mathcal{P}_m is independent of $\sigma_{8,0}$ (it gives the shape of the power spectrum).

The Fisher matrix in our case is a 2×2 symmetric matrix:

$$F_{\alpha\beta} = \begin{pmatrix} F_{\gamma\gamma} & F_{\gamma\sigma_{8,0}} \\ F_{\sigma_{8,0}\gamma} & F_{\sigma_{8,0}\sigma_{8,0}} \end{pmatrix}. \quad (5.6)$$

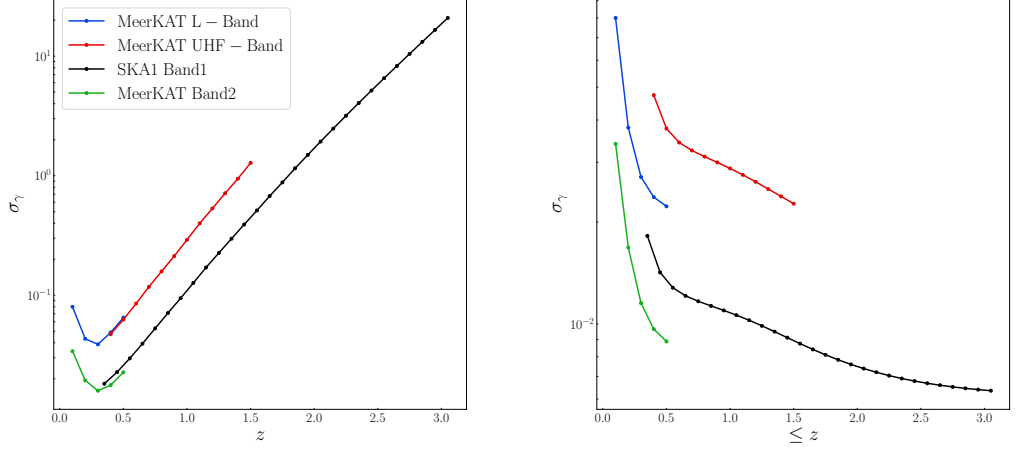


FIGURE 5.1: For MeerKAT and SKA: the forecast marginalized errors for γ , per redshift bin (*left*) and cumulative (*right*).

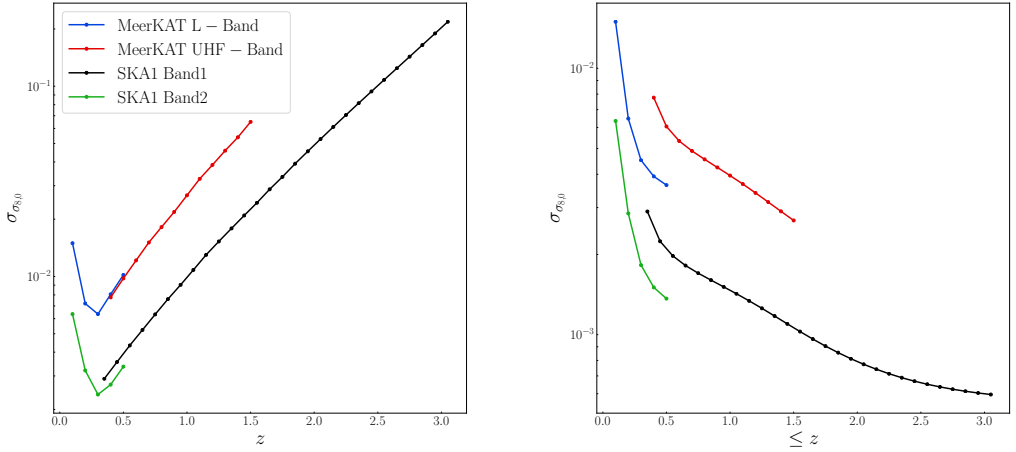


FIGURE 5.2: For MeerKAT and SKA: the forecast marginalized errors for $\sigma_{8,0}$, per redshift bin (*left*) and cumulative (*right*).

We invert \mathbf{F} to obtain the covariance matrix [35, 36]:

$$C_{\alpha\beta} = (\mathbf{F}^{-1})_{\alpha\beta} = \begin{pmatrix} \sigma_{\gamma\gamma} & \sigma_{\gamma\sigma_{8,0}} \\ \sigma_{\sigma_{8,0}\gamma} & \sigma_{\sigma_{8,0}\sigma_{8,0}} \end{pmatrix}, \quad (5.7)$$

where the marginalized errors are the diagonal elements: $\sigma_\alpha \equiv \sigma_{\alpha\alpha}$. The off-diagonal elements give the correlation between the parameters.

For the power spectrum model, we use the exponential FoG damping factor. Using Python we compute the Fisher matrix for each experiment, using the survey specifications (Table 4.1) and other information in Chapter 4 to compute the variance. Then we invert the matrix to get the marginalized errors.

Figures 5.1 and 5.2 show the per-bin and the cumulative marginal errors for MeerKAT and SKA. As expected, SKA delivers greater precision than MeerKAT.

5.2 Extended MeerKAT

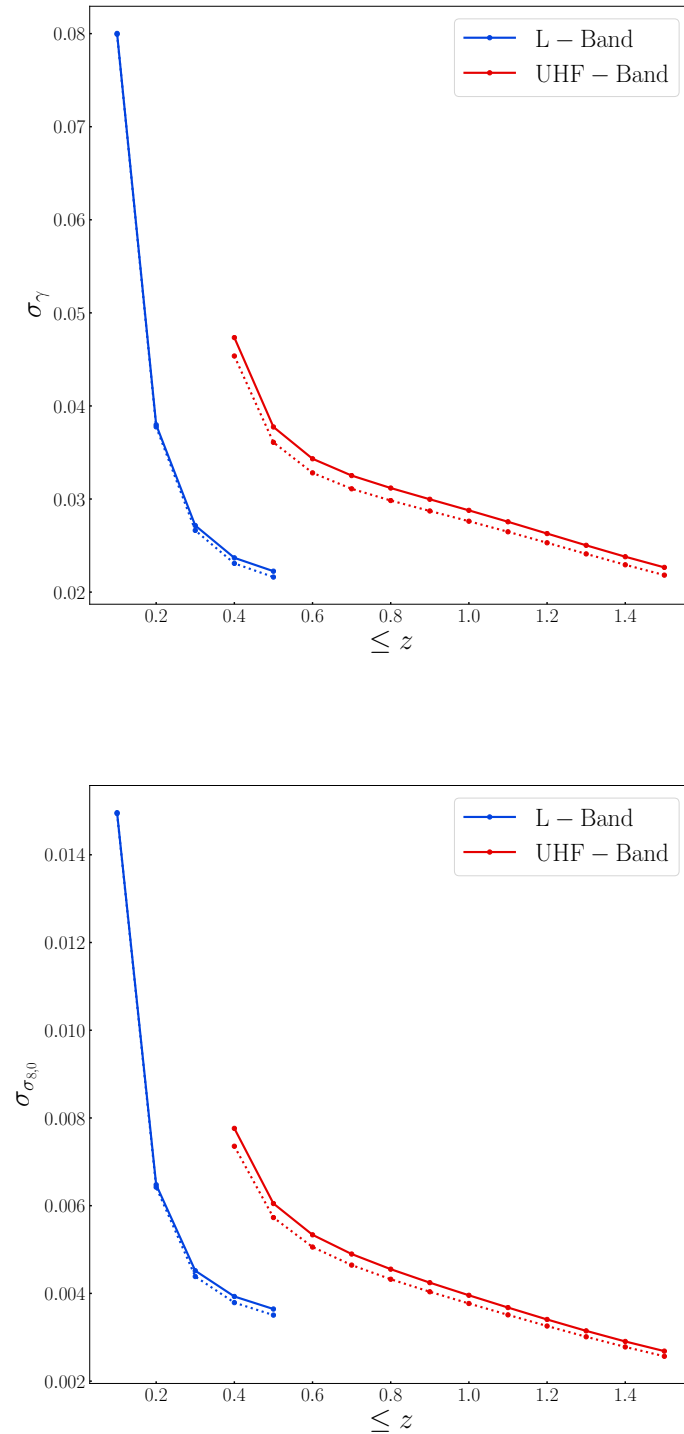


FIGURE 5.3: The dotted lines show the improvement in marginalised errors compared to Figures 5.1 and 5.2 with $N_d = 84$ dishes in MeerKAT.

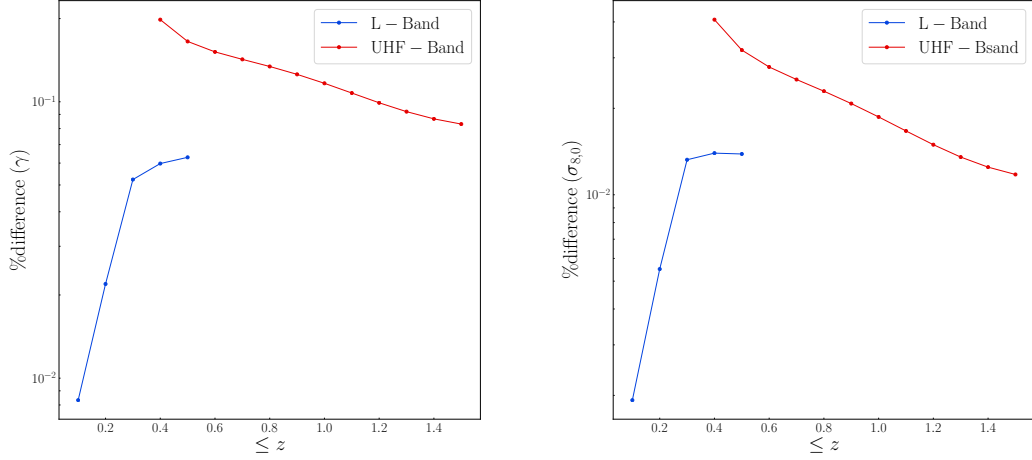


FIGURE 5.4: The percentage difference between MeerKAT of 64 and extend MeerKAT of 84 dishes.

MeerKAT will be extended by an extra 20 dishes before it is integrated into SKA; see

<https://www.mpifr-bonn.mpg.de/pressreleases/2020/9>

In Figure 5.4, we present the Fisher forecasts of the MeerKAT (with $N_d = 64$ dishes, solid lines) and Extension ($N_d = 84$ dishes, dotted lines). The MeerKAT Extension gives better constraints compared to MeerKAT. However, as shown in Figure 5.3, the improvement is not large.

5.3 Normalized Marginal Errors

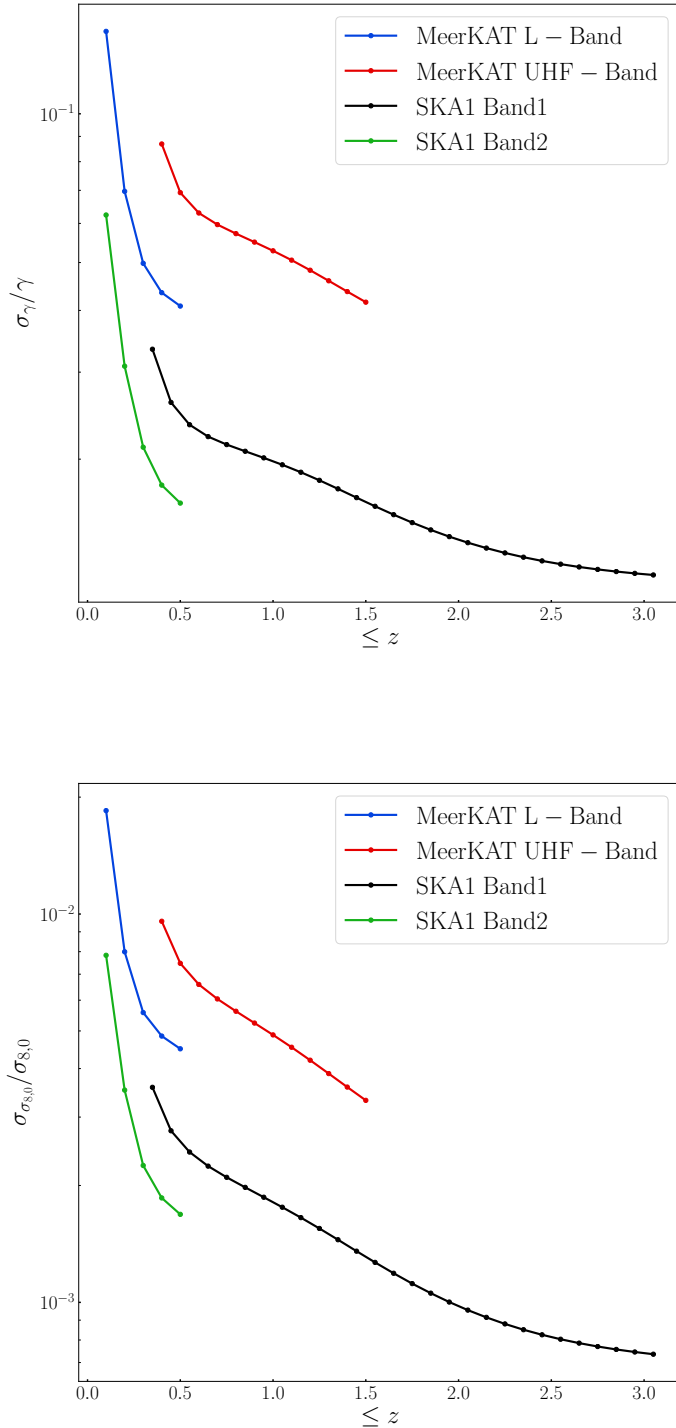


FIGURE 5.5: For MeerKAT and SKA: normalized marginal errors on γ and $\sigma_{8,0}$.

After getting cumulative marginalized errors on γ and $\sigma_{8,0}$ from these two surveys, we divided the errors by the fiducial values to give the normalised errors. The results are shown in Figure 5.5. We see that the precision on γ is a few percent (but over 10% for the first bin of MeerKAT L-band). For $\sigma_{\sigma_{8,0}}$, the precision is sub-percent (but a few percent for the first bin of MeerKAT L-band).

We also present the total normalized cumulative marginal errors – i.e. the cumulative normalized marginal error at the maximal redshift bin z_{max} – in Table 5.1.

Survey	σ_γ/γ	$\sigma_{\sigma_{8,0}}/\sigma_{8,0}$
MeerKAT L-Band	0.147	0.018
MeerKAT UHF-Band	0.099	0.011
MeerKAT L-Band-84	0.147	0.018
MeerKAT UHF-Band-84	0.095	0.010
SKA1 Band1	0.033	0.004
SKA1 Band2	0.062	0.009

TABLE 5.1: Total normalized marginal errors for both γ and $\sigma_{8,0}$ parameters from each survey at maximal redshift z_{max} . We also showed the normalization of MeerKAT with 84 dishes.

Chapter 6

Conclusions and Future Work

In this Chapter is the summary of the thesis and its main results, together with a brief discussion of future work.

6.1 Summary

Chapter 1 is an introductory review of the background cosmology model of the universe with important equations that describe the expanding Friedmann-Robertson-Walker universe and its basic properties.

Chapter 2 describes the formalism and applications of linear perturbations around the FLRW background, in order to understand the evolution of fluctuations that are initially seeded by Inflation. Specifically, we focus on the matter density contrast and how it evolves to generate the large-scale structure. We describe how galaxy number counts and HI intensity fluctuations relate to the corresponding density fluctuations. We analyse the peculiar velocity of matter and the relation between it, the density contrast and the gravitational potential. This is the basis for the analysis of redshift space distortions in Chapter 3.

RSD causes an enhancement of large-scale clustering along the line of sight, shown in Figure 3.1. To see how the RSD impacts the HI power spectrum, see Figure 3.4,

showing how the HI power spectrum behaves in real space and redshift space. The aim is to test gravity on large scales by measuring the growth rate of large-scale structure via the HI intensity mapping power spectrum in redshift space.

To model the HI intensity power spectrum we start with a simple linear model of RSD as explained in Section 3.1 and then extend to nonlinear models of the RSD in Section 3.2, using the Finger of God (FoG) model with damping parameter $\sigma(z)$, as in (3.18). Various FoG models can be used, shown in (3.17) and Figure 3.7, but we choose to use the Gaussian damping factor, following the model of [37].

The RSD HI power spectrum of linear (Figure 3.3) and non-linear (Figure 3.5) models can be described using a multipole expansion. Three multipoles ($\ell = 0, 1, 2$) are enough to describe the linear models.

The research results of this thesis reported in Chapters 4 and 5.

Accurate measurements of the growth rate for HI intensity mapping surveys on the radio telescope arrays MeerKAT and SKA1 (single-dish mode) require a high signal to noise ratio [see (4.12)] on the redshift space power spectrum. Figure 4.8 confirm that the SNR is high in both cases. The SNR is significantly reduced by the effect of the telescope beam, and also at a lower level by the effects of foreground cleaning. The foreground cleaning removes the large-scale radial modes while the beam damps the small-scale angular modes, as seen in (4.1) and (4.4) respectively.

From Figure 4.8 we find that we have enough signal to noise in both surveys on the power spectrum. This lead us to predict the errors on the growth index $\gamma = \ln f / \ln \Omega_m$, which is the parameter that is needed for testing gravity. In standard general relativity, $\gamma = 0.545$, which we use as our fiducial in Fisher forecasts. To estimate the precision with which MeerKAT and SKA can constrain γ , we perform a Fisher analysis with two parameters, γ and $\sigma_{8,0}$, in (5.1).

The results for marginalised errors (per redshift bin and cumulative) are shown in Figures 5.1 and 5.2. We also plot the normalised marginal errors in Figure 5.5 and present the total errors in Table 5.1. Our results show that MeerKAT and SKA

predict to achieve percent-level precision on γ and sub-percent precision on $\sigma_{8,0}$. SKA clearly outperforms MeerKAT as expected, and the best constraints come from Band 1 and UHF-band, i.e., the bands reaching the highest redshifts and therefore the largest volumes. Our constraints assume that the standard cosmological parameters are already measured by existing experiments. In addition, we fix the HI bias and the FoG damping parameter. A more realistic forecast would include these parameters in the Fisher analysis.

We also look at the constraints from extended MeerKAT, with 20 additional dishes, shown in Figure 5.3 and Table 5.1. The improvement over MeerKAT is not large.

6.2 Future Work

Future work will start by extending the Fisher analysis of MeerKAT and SKA to include some of the standard cosmological parameters, such as h , Ω_{m0} , n_s , and the two astrophysical parameters $b_{\text{HI}}(z)$ and $\sigma(z)$. Then we could extend the analysis to the HIRAX and PUMA surveys in interferometer mode [38].

We should also include the Alcock-Paczynski effect in our forecasts, arising from an incorrect choice of fiducial cosmological model [39, 40]. This would enable us to simultaneously forecast the precision on $H(z)$ and $d_A(z)$. Also we could look at the primordial non-Gaussianity parameter f_{NL} , by including scale-dependent clustering bias in the power spectrum.

A further extension would be to investigate the combination of 21cm intensity maps with other galaxy surveys to enhance precision and suppress systematics. Finally, we could include the HI intensity mapping bispectrum, in order to break parameter degeneracies.

Bibliography

- [1] B. Ryden, *Introduction to cosmology*. Cambridge University Press, 1, 2005.
- [2] S. Dodelson, *Modern Cosmology*. Academic Press, Amsterdam, 2003.
- [3] L. Amendola and S. Tsujikawa, *Dark Energy: Theory and Observations*. Cambridge University Press, 1, 2015.
- [4] V. Mukhanov, *Physical Foundations of Cosmology*. Cambridge University Press, Oxford, 2005.
- [5] P. Peter and J.-P. Uzan, *Primordial Cosmology*. Oxford Graduate Texts. Oxford University Press, 2, 2013.
- [6] G. F. R. Ellis, R. Maartens, and M. A. H. MacCallum, *Relativistic Cosmology*. Cambridge University Press, 2012.
- [7] **Planck** Collaboration, N. Aghanim et al., *Planck 2018 results. VI. Cosmological parameters*, [arXiv:1807.06209](https://arxiv.org/abs/1807.06209).
- [8] C. Burgess, *Intro to Effective Field Theories and Inflation*, [arXiv:1711.10592](https://arxiv.org/abs/1711.10592).
- [9] T. Rindler-Daller, *Understanding CMB physics through the exploration of exotic cosmological models: a classroom study using CLASS*, *Eur. J. Phys.* **41** (2020), no. 3 035602, [[arXiv:1908.05042](https://arxiv.org/abs/1908.05042)].
- [10] J. Lesgourgues, *The cosmic linear anisotropy solving system (class) i: Overview*, [arXiv:1104.2932](https://arxiv.org/abs/1104.2932).

- [11] T. Padmanabhan, *Advanced topics in cosmology: a pedagogical introduction*, *AIP Conf. Proc.* **843** (2006), no. 1 111–166, [[astro-ph/0602117](#)].
- [12] D. Baumann, *Primordial Cosmology*, *PoS TASI2017* (2018) 009, [[arXiv:1807.03098](#)].
- [13] O. F. Piattella, *Lecture Notes in Cosmology*. UNITEXT for Physics. Springer, Cham, 2018.
- [14] R. Maartens, *Theoretical Cosmology MSc Notes 2018* , .
- [15] **MeerKCLASS** Collaboration, M. G. Santos et al., *MeerKCLASS: MeerKAT Large Area Synoptic Survey*, [arXiv:1709.06099](#).
- [16] O. Umeh, R. Maartens, and M. Santos, *Nonlinear modulation of the HI power spectrum on ultra-large scales. I*, *JCAP* **03** (2016) 061, [[arXiv:1509.03786](#)].
- [17] M. G. Santos et al., *Cosmology from a SKA HI intensity mapping survey*, *PoS AASKA14* (2015) 019, [[arXiv:1501.03989](#)].
- [18] W. J. Percival and M. White, *Testing cosmological structure formation using redshift-space distortions*, *Mon. Not. Roy. Astron. Soc.* **393** (2009) 297, [[arXiv:0808.0003](#)].
- [19] A. Hamilton, *Linear redshift distortions: A Review*, in *Ringberg Workshop on Large Scale Structure*, 8, 1997. [astro-ph/9708102](#).
- [20] S. Saito, *Galaxy Clustering in Redshift Space*, 6, 2016.
- [21] V. Tansella, C. Bonvin, R. Durrer, B. Ghosh, and E. Sellentin, *The full-sky relativistic correlation function and power spectrum of galaxy number counts. Part I: theoretical aspects*, *JCAP* **03** (2018) 019, [[arXiv:1708.00492](#)].
- [22] F. Villaescusa-Navarro et al., *Ingredients for 21 cm Intensity Mapping*, *Astrophys. J.* **866** (2018), no. 2 135, [[arXiv:1804.09180](#)].

- [23] D. Sarkar and S. Bharadwaj, *Modelling redshift space distortion in the post-reionization H i 21-cm power spectrum*, *Mon. Not. Roy. Astron. Soc.* **476** (2018), no. 1 96–108, [[arXiv:1801.07868](https://arxiv.org/abs/1801.07868)].
- [24] S. Cunnington, A. Pourtsidou, P. S. Soares, C. Blake, and D. Bacon, *Multipole expansion for HI intensity mapping experiments: simulations and modelling*, [arXiv:2002.05626](https://arxiv.org/abs/2002.05626).
- [25] S. Bharadwaj, *Radial Redshift Space Distortions*, *Astrophys. J.* **516** (1999) 507–518, [[astro-ph/9812274](https://arxiv.org/abs/astro-ph/9812274)].
- [26] H. Magira, Y. Jing, and Y. Suto, *Cosmological redshift-space distortion on clustering of high-redshift objects: correction for nonlinear effects in power spectrum and tests with n-body simulations*, *Astrophys. J.* **528** (2000) 30, [[astro-ph/9907438](https://arxiv.org/abs/astro-ph/9907438)].
- [27] E. Majerotto et al., *Probing deviations from General Relativity with the Euclid spectroscopic survey*, *Mon. Not. Roy. Astron. Soc.* **424** (2012) 1392–1408, [[arXiv:1205.6215](https://arxiv.org/abs/1205.6215)].
- [28] N. Kaiser, *Clustering in real space and in redshift space*, *Mon. Not. Roy. Astron. Soc.* **227** (1987) 1–27.
- [29] W. L. W. Sargent and E. L. Turner, *A statistical method for determining the cosmological density parameter from the redshifts of a complete sample of galaxies.*, .
- [30] P. Bull, P. G. Ferreira, P. Patel, and M. G. Santos, *Late-time cosmology with 21cm intensity mapping experiments*, *Astrophys. J.* **803** (2015), no. 1 21, [[arXiv:1405.1452](https://arxiv.org/abs/1405.1452)].
- [31] S. Jolicoeur, R. Maartens, E. M. De Weerd, O. Umeh, C. Clarkson, and S. Camera, *Detecting the relativistic bispectrum in 21cm intensity maps*, [arXiv:2009.06197](https://arxiv.org/abs/2009.06197).
- [32] J. Fonseca, J.-A. Viljoen, and R. Maartens, *Optimal constraints on the growth rate using the observed galaxy power spectrum*, [arXiv:1907.02975](https://arxiv.org/abs/1907.02975).

- [33] D. Karagiannis, A. Lazanu, M. Liguori, A. Raccanelli, N. Bartolo, and L. Verde, *Constraining primordial non-Gaussianity with bispectrum and power spectrum from upcoming optical and radio surveys*, *Mon. Not. Roy. Astron. Soc.* **478** (2018), no. 1 1341–1376, [[arXiv:1801.09280](https://arxiv.org/abs/1801.09280)].
- [34] V. Yankelevich and C. Porciani, *Cosmological information in the redshift-space bispectrum*, *Mon. Not. Roy. Astron. Soc.* **483** (2019), no. 2 2078–2099, [[arXiv:1807.07076](https://arxiv.org/abs/1807.07076)].
- [35] D. Coe, *Fisher matrices and confidence ellipses: A quick-start guide and software*, [arXiv:0906.4123](https://arxiv.org/abs/0906.4123).
- [36] A. Albrecht, L. Amendola, G. Bernstein, D. Clowe, D. Eisenstein, L. Guzzo, C. Hirata, D. Huterer, R. Kirshner, E. Kolb, and R. Nichol, *Findings of the joint dark energy mission figure of merit science working group*, [arXiv:0901.0721](https://arxiv.org/abs/0901.0721).
- [37] S. Bharadwaj, *Nonlinear redshift distortions: The Two point correlation function*, *Mon. Not. Roy. Astron. Soc.* **327** (2001) 577–587, [[astro-ph/0105320](https://arxiv.org/abs/astro-ph/0105320)].
- [38] D. Karagiannis, A. Slosar, and M. Liguori, *Forecasts on Primordial non-Gaussianity from 21 cm Intensity Mapping experiments*, [arXiv:1911.03964](https://arxiv.org/abs/1911.03964).
- [39] X. Luo, Z. Wu, X.-D. Li, M. Li, Z. Li, and C. G. Sabiu, *Cosmological constraints from the redshift dependence of the Alcock-Paczynski effect: Fourier space analysis*, [arXiv:1908.10593](https://arxiv.org/abs/1908.10593).
- [40] F. Lepori, E. Di Dio, M. Viel, C. Baccigalupi, and R. Durrer, *The Alcock Paczyński test with Baryon Acoustic Oscillations: systematic effects for future surveys*, *JCAP* **02** (2017) 020, [[arXiv:1606.03114](https://arxiv.org/abs/1606.03114)].